High-resolution finite element methods for 3D simulation of compositionally triggered instabilities in porous media

Ebrahim Shahraeeni, Joachim Moortgat & Abbas Firoozabadi

Computational Geosciences
Modeling, Simulation and Data Analysis

ISSN 1420-0597

Comput Geosci
DOI 10.1007/s10596-015-9501-z

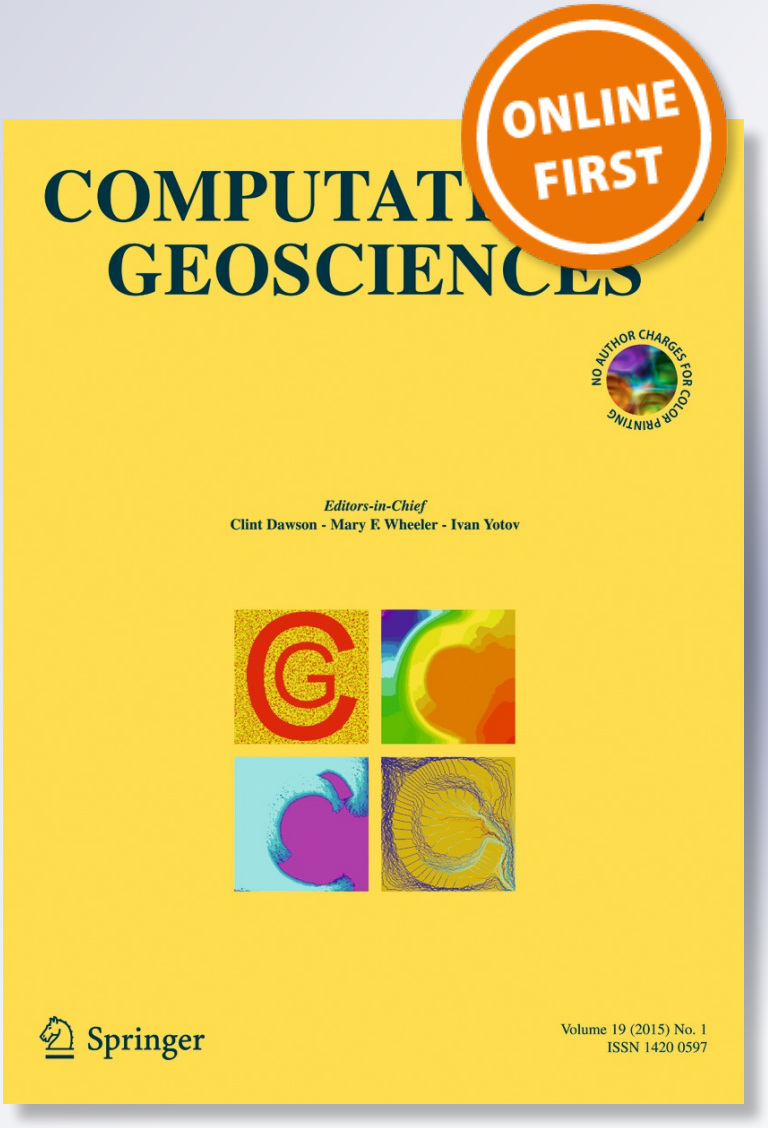

Springer

Your article is protected by copyright and all rights are held exclusively by Springer International Publishing Switzerland. This e-offprint is for personal use only and shall not be self-archived in electronic repositories. If you wish to self-archive your article, please use the accepted manuscript version for posting on your own website. You may further deposit the accepted manuscript version in any repository, provided it is only made publicly available 12 months after official publication or later and provided acknowledgement is given to the original source of publication and a link is inserted to the published article on Springer's website. The link must be accompanied by the following text: "The final publication is available at link.springer.com”.

Author's personal copy

Comput Geosci
DOI 10.1007/s10596-015-9501-z

ORIGINAL PAPER

High-resolution finite element methods for 3D simulation of compositionally triggered instabilities in porous media

Ebrahim Shahraeeni[1] · Joachim Moortgat[2] · Abbas Firoozabadi[1,3]

Received: 20 August 2014 / Accepted: 4 May 2015
© Springer International Publishing Switzerland 2015

Abstract The formation and development of patterns in the unstable interface between an injected fluid and hydrocarbons or saline aqueous phase in a porous medium can be driven by viscous effects and gravity. Numerical simulation of the so-called fingering is a challenge, which requires rigorous representation of the fluid flow and thermodynamics as well as highresolution discretization in order to minimize numerical artifacts. To achieve such a high resolution, we present higherorder 3D finite element methods for the simulation of fully compositional, three-phase and multi-component flow. This is based on a combination of the mixed hybrid finite element (MHFE) method for total fluid velocity and discontinuous Galerkin (DG) method for the species transport. The phase behavior is described by cubic or cubic-plus-association (CPA) equations of state. We present challenging numerical examples of compositionally triggered fingering at both the core and the large scale. Four additional test cases illustrate the robustness and efficiency of the proposed methods, which demonstrate their power for problems of this complexity. Results reveal three orders of magnitude improvement in CPU time in our method compared with the lowest-order finite difference method for some of the examples. Comparison between 3D and 2D results highlights the significance of dimensionality in the flow simulation.

Keywords Gravitational fingering · Mixed hybrid finite element methods · Multiphase and multicomponent flow · 3D simulation · Compositional modeling

Mathematics Subject Classification (2010) 76T30 · 76S05 · 65M60 (from 1)

1 Introduction

Accurate numerical simulation of CO_2 injection in hydrocarbon reservoirs is a challenge. Transfer of species between the phases alters the phase densities, viscosities and composition of the fluids and results in phase changes, swelling or shrinkage and the possibility of instabilities. These processes drive secondorder patterns of fluid flow in the domain Fingering generally refers to the onset and evolution of instabilities that occur in the displacement of fluid in porous materials. It results from variations in either viscosity or density between phases or within a singlephase containing a solute [1]. Fingering may drastically affect fluid flow in porous media and thus impact enhanced oil recovery or sequestration performance; for which they are intensively studied numerically and experimentally [1–11].

For the numerical simulation of phenomena such as fingering, from one side rigorous representation of the source of complexity (i.e., fluid mechanics and thermodynamics of the processes) is essential and from the other side

✉ Ebrahim Shahraeeni
e.shahraeeni@gmail.com

Joachim Moortgat
moortgat.1@osu.edu

Abbas Firoozabadi
Firoozabadi@Yale.edu

[1] Reservoir Engineering Research Institute (RERI), Palo Alto, CA 94301, USA

[2] School of Earth Sciences, The Ohio State University, Columbus, OH 43210, USA

[3] Yale School of Engineering and Applied Science, New Haven, CT 06511, USA

Published online: 30 May 2015

Author's personal copy

highresolution numerical discretization is required in order to minimize numerical dispersion, which otherwise obscures small-scale patterns. The performance of a numerical code for the simulation of compositional flow in porous media is a compromise between accuracy and speed. Different logics are implemented to balance this trade-off, which has resulted in a series of algorithms for compositional modeling in the literature. A review of some of the available codes has been presented by Class et al. [12]. They can be separated into two main categories according to the basic equations for mass balance or volume balance. Different choices of primary variables may be mathematically and physically equivalent, but may result in different numerical behavior. Two categories of numerical formulations are fully implicit methods and implicit pressure, explicit composition (IMPEC) methods [13]. Fully implicit methods are numerically stable but they lead to large matrices, which consequently limit the CPU efficiency by the number of components. They also generally exhibit higher numerical dispersion than the IMPEC approach. To reduce the level of implicitness and thus solve smaller linear systems, the problem can be reformulated into a pressure equation and mass conservation equations [14]. The overall technique is called the IMPEC procedure, which is limited by stability restrictions on the time step size. Seeking for higher efficiency, an intermediate degree of implicitness is also possible with techniques like implicit pressure and saturation (IMPSAT) or adaptive implicit (AIM) [15]. A few of the compositional simulators are developed in the framework of commercial software used extensively in the industry [16, 17]. Both commercial packages GEM (by CMG) and ECLIPSE (by Schlumberger) use the integrated finite difference method (IFDM) for the spatial discretization and either an implicit or an explicit Euler scheme for time integration. Among research codes, DuMux developed at the University of Stuttgart, uses a BOX scheme for space discretization while the time integration is performed via a standard implicit Euler scheme [18]. FEHM has been developed since early 1970s at the Los Alamos National Laboratory and is based on a control volume finite element (CVFE) spatial discretization approach and an implicit time discretization [19]. Stanford University's finite volume (FV) based GPRS initially developed by Cao [20] and further extended by Jiang [21] supports varying degrees of implicitness for time discretization. IPARS is being developed at the Center for Subsurface Modeling (CSM) at the University of Texas at Austin [22–25], which uses an iteratively coupled sequential IMPEC algorithm for the saturations. The pressure equation is solved using a backward Euler method for time discretization and mixed FEM for space discretization. TOUGH2 developed at the Lawrence Berkeley National Laboratory uses integrated finite difference method (IFDM) for discretization in space and implicit time integration [26]. One last approach to resolve small-scale features is to use adaptive mesh refinement (AMR) as described e.g. in [27] and were implemented in [10]. Similar approach is used by NORMS group from Imperial College [28, 29]. These research codes are examples for different fields of application.

In compositional modeling, numerical dispersion tends to smooth sharp composition and saturation fronts. The degree of numerical dispersion depends on the order of method used in the discretization. There are inherent limitations in zeroth-order methods, where steep gradients in compositions and transport properties cannot be captured accurately by element-wise constant values, unless an exceedingly fine mesh is used Higher-order methods, on the other hand, yield more accurate approximations of the sharp fronts because they include additional terms in the estimation of gradients. The memory and computational costs of grid refinement for a lowest-order method far outweigh the overhead from a higher-order method in achieving comparable accuracy. Higher-order and mimetic finite difference and finite volume methods which have been extensively discussed in the literature [30–32] often rely on information from further neighboring grid blocks. In contrast, higher-order finite element methods achieve better estimation locally within the grid block by increasing the degree of freedom in the approximation of variables inside the element. This flexibility provided by the higher-order finite element methods is particularly important in highly heterogeneous domains where information from further neighboring elements may result in strong additional nonlinearity in the system if higher-order finite volume or finite difference methods are used.

Higher-order finite element methods are computationally more expensive per element and require careful implementation [33]. But these methods have advantages in the representation of complex physical processes like viscous and gravitational fingering where reducing numerical dispersion is critical. To capture such effects with lowerorder methods finer mesh should be used, which drastically increases total simulation time This motivates the implementation of higher-order methods for such applications. Following the same line of reasoning, the extension to even higher-order spatial discretization in the transport of a singlephase problem is an option, although, as it will be explained in the following sections, for multiphase flow, due to the increase of expensive phase-split calculations required for each degree of freedom, determining whether the additional accuracy from higher-orders justifies the additional cost is not trivial.

Dimensionality is another issue of concern in the simulation of fingering processes. Gravitational and viscous fingers are 3D in nature and 2D representation of them might lead to significant discrepancy between the numerical results and experimental data. Truncation error induced

Author's personal copy

by numerical dispersion in a solution is indeed affected by the problem dimension. Extra dimensions result in higher numerical dispersion. In an early paper, Coats [34] showed significant numerical dispersion in the zero-order methods for 1D problem. Later Ewing and Heinemann [35] compared numerical dispersion in 2D. In a 3D domain, whether in zeroth-order or in higher-order methods, one expects more pronounced numerical dispersion compared with 1D and 2D. The main objective of this work is to develop the algorithm for the combined DG and MHFE methods in 3D to study gravitational fingering for three-phase compositional and compressible flow. The performance will be evaluated in comparison with lower-order and lower-dimension results in a series of illustrative examples.

We consider two sources of gravitational flow instabilities (fingering) in compositional flow. In the first, a denser liquid is injected on top of a lighter liquid. Specifically, we consider reservoir conditions at which injected CO_2 is supercritical and denser than the oil in the saturated porous medium, resulting in unstable flow. In the second case, CO_2 is injected from the top with a lower density than the reservoir fluid, but it dissolves in the reservoir fluid and this dissolution increases the local liquid density in the top, which is again unstable. We consider two scenarios where this may occur. One is dissolution of injected CO_2 into oil, and the second is in the context of CO_2 sequestration in aquifers where CO_2 may dissolve into the aqueous phase. In both cases, the density increase from CO_2 dissolution may only be a (few) percent, but for high-permeability formations this is sufficient to trigger gravito-convective mixing of dissolved CO_2 throughout the reservoir or aquifer at a *convective* rate that is much faster than diffusive transport of CO_2.

Fickian diffusion plays a critical two-fold role in this process. First, Fickian diffusion is what drives the initial dissolution of CO_2 from the gas phase into the oil or aqueous phase. This process occurs across the phase boundary and can be relatively fast even for small diffusion coefficients (unlike diffusive transport over reservoir scales). Second, Fickian diffusion acts as a restoring force at the onset of gravitational flow instabilities (fingering). Once a finger starts to develop, this sets up compositional gradients that will drive diffusion of CO_2 from the elevated-CO_2-concentration fingers to the low-CO_2-concentration ambient oil or aqueous phase. This process "smears out" or stabilizes the instability. Higher diffusion coefficients will delay the onset of gravitational fingers (critical time) and result in fewer and larger fingers (critical wavelength) when the instability does develop.

The density difference between CO_2enriched versus CO_2-free phases is the driver for fingering, while the convective rate of finger growth is governed by Darcy's law, and thus proportional to the formation permeability and inversely proportional to viscosity. Linear stability analyses have been carried out to determine at what critical time and wavelength the unstable density difference will exceed the diffusive stabilizing force (e.g., [10, 36–39] and references therein). The onset time and critical wavelength depend on the aforementioned reservoir and fluid properties, but different stability analyses and simulation studies find a wide range in overall proportionality constants. In [40], we simulated 2D fingering behavior in an aquifer and found a proportionality factor close to that in [10]. In this work we simulate both a 3D example from [10] for single-phase flow in a CO_2 sequestration context, as well as unfavorable fingering for multiphase flow in an oil reservoir, which was modeled before with CMG [16].

We advance the modeling of fingering in 3D by (1) the use of higher-order methods, which can capture the small-scale onset of the instability on relatively coarse grids, (2) a self-consistent model for Fickian diffusion in multi-component multiphase mixtures [41], and (3) accurate fluid properties from equation of state (EOS)-based phase stability and phase-split computations for two- and three-phase flow. We rely on the commonly used Peng-Robinson EOS for pure hydrocarbon phases, but use a more accurate cubic-plus-association EOS for mixtures that contain polar components [40]. The latter is most important for the aqueous phase in the context of carbon sequestration studies.

Following this brief introduction, in the next section we present the mathematical formulation of the problem. Derivations of the discretized form of the equations in 3D are briefly presented in the Section 3. In the Section 4 we discuss the rate of convergence, accuracy and CPU time of zero-order and higher-order methods in 3D problems. We also compare 2D and 3D results to investigate the effect of dimension reduction on flow and species transport in challenging cases where fingers form due to the compositional effects. The paper is summarized with concluding remarks.

2 Mathematical formulation

In this section, we briefly summarize the formulation for compositional modeling of higher-order methods in 3D. We first discuss the species transport, and then the flow equations.

2.1 Species transport

The mass balance of each species is given by

$$\phi \frac{\partial c z_i}{\partial t} + \nabla \cdot \mathbf{U}_i = F_i \quad i = 1, 2, ..., n_c \tag{1}$$

Author's personal copy

where φ [−] is porosity (assumed constant), c[mol/m^3] is overall molar density, z_i[−] is overall mole fraction of component i ($\Sigma_i z_i = 1$), t [s] is time, $\mathbf{U_i}$ [mol/m^2/s] is total molar flux of component i and F_i [mol/m^3/s] is the distribution of sources/sinks of component i. The total molar flux $\mathbf{U}_i$ is the sum of convective and diffusive fluxes:

$$\mathbf{U}_i = \sum_{\alpha} (c_\alpha x_{\alpha i} \mathbf{v}_\alpha + S_\alpha \mathbf{J}_{\alpha i}) \quad i = 1, 2, ..., n_c, \ \alpha = o, g, w. \tag{2}$$

The diffusive flux $\mathbf{J}_{\alpha i}$ can be expressed by

$$\mathbf{J}_{\alpha i} = -c_\alpha \phi \sum_{j=1}^{n_c-1} D_{\alpha ij} \nabla x_{\alpha j} \quad i = 1, 2, ..., n_c - 1$$

$$\sum_{j=1}^{n_c} \mathbf{J}_{\alpha j} = 0 \tag{3}$$

where the subscript $\alpha = o, g$ and w denotes the oil, gas and water phases, respectively, with α designating a generic phase, c_α[mol/m^3] is the molar density of phase α, $x_{\alpha I}$[mole fraction] is the mole fraction of component i in phase α ($\Sigma_\alpha x_{\alpha i} = 1$), $\mathbf{v}_\alpha$ [m/s] is the (effective) velocity vector of phase α, S_α [−] the saturation of phase α and $\mathbf{J}_{\alpha i}$ [mol/m^2/s] is the diffusive flux of component i in phase α. The Fickian diffusion coefficient matrix with elements $D_{\alpha ij}$ is computed using the unified model from Leahy-Dios and Firoozabadi [42].

2.2 Darcy's law

Darcy's law gives the phase velocity as

$$\mathbf{v}_\alpha = -\lambda_\alpha \underline{K} (\nabla p - \rho_\alpha \mathbf{g}) \tag{4}$$

where $\mathbf{v}_\alpha$ [m/s] is phase velocity, p[Pa] is pressure, ρ_α [kg/m^3] is mass density of phase α, $\mathbf{g}$ [kg/m/s^2] is gravity acceleration, $\underline{K}$ [m^2] is medium intrinsic permeability tensor, and λ_α [m.s/kg] is the phase mobility. In the numerical implementation of the method for the sake of simplicity, we assume an isotropic domain with scalar (yet heterogeneous) permeability $\underline{K}$.

The mass density of phase α is calculated from:

$$\rho_\alpha = c_\alpha \sum_{i=1}^{n_c} x_{\alpha i} M_i \quad \alpha = o, g, w \tag{5}$$

where M_i [g/mol] is the molecular weight of component i.

The phase mobility (λ_α) is a function of phase saturation(s) (S_αg[−]), relative permeability $k_{r\alpha}$ [−] and phase viscosity μ_α [kg/m/s]. The phase mobility is defined as $\lambda_\alpha(S_\alpha) = k_{r\alpha}/\mu_\alpha$.

We use the total velocity as the primary unknown in Darcy's law [43, 44], which is a smooth function of space and adds both accuracy and robustness to the computations. Another advantage of using the total velocity relates to cases where a phase disappears; the phase mobility λ_α will then be zero, which result in zero phase velocity. But with total velocity $\mathbf{v}$

$$\mathbf{v} \equiv \mathbf{v}_w + \mathbf{v}_g + \mathbf{v}_o \tag{6}$$

as long as one of the phases is mobile, the total velocity $\mathbf{v}$ is non-zero and the system of equations is positive definite and solvable for pressure.

Defining total mobility λ_t, total mass density ρ and fractional flow functions f_α as

$$\lambda_t = \sum_{\alpha} \lambda_\alpha, \ \rho = \sum_{\alpha} f_\alpha \rho_\alpha, \ f_\alpha = \frac{\lambda_\alpha}{\lambda_t}, \tag{7}$$

we write the total velocity as

$$\mathbf{v} = -\sum_{\alpha} \lambda_\alpha \underline{K} (\nabla p - \rho_\alpha \mathbf{g}) = -\lambda_t \underline{K} (\nabla p - \rho \mathbf{g}). \tag{8}$$

From Eq. 8, the pressure gradient ∇p is obtained:

$$\nabla p = -\frac{\underline{K}^{-1}}{\lambda_t} \mathbf{v} + \rho \mathbf{g}. \tag{9}$$

Introducing (9) into Darcy's equation (4) yields the phase velocity $\mathbf{v}_\alpha$ as a function of the total velocity $\mathbf{v}$:

$$\mathbf{v}_\alpha = f_\alpha (\mathbf{v} + \mathbf{G}_\alpha) \quad \mathbf{G}_\alpha = \underline{K} \mathbf{g} \sum_{\beta = o,g,w} \lambda_\beta (\rho_\alpha - \rho_\beta). \tag{10}$$

2.3 Pressure equation

Using the concept of volume-balance [45], one can derive the following pressure equation:

$$\phi C_f \frac{\partial p}{\partial t} + \sum_{i=1}^{n_c} \bar{v}_i \nabla \cdot (c_o x_{oi} \mathbf{v}_o + S_o \mathbf{J}_{oi} + c_g x_{gi} \mathbf{v}_g + S_g \mathbf{J}_{gi} + c_w x_{wi} \mathbf{v}_w + S_w \mathbf{J}_{wi}) = \sum_{i=1}^{n_c} \bar{v}_i F_i \tag{11}$$

where C_f[m.s^2/kg] is the total compressibility and $\bar{v}_I$[m^3/mol] is the total partial molar volume of component i. Moortgat et al. [46] outline the procedure for the computation of C_f and $\bar{v}_I$ in three-phase gas-oil-water mixture.

2.4 Thermodynamic equilibrium relations

For successful largescale compositional simulations, an efficient and robust phase equilibrium computational algorithm is required. Li and Firoozabadi [47] present an efficient strategy for stability analysis and phase-split calculations. In three-phase, the component splitting between phases is carried out by solving thermodynamic equilibrium equations based on the equality of phase fugacities. For a given set of pressure p, temperature T and overall composition z_i of a

Author's personal copy

system with n_c components, one may calculate phase compressibility factor Z_α and phase composition $x_{i,\alpha}$. Details of the calculation are provided by Li and Firoozabadi [47]. We adopt the Peng-Robinson equation of state (EOS) [48] for hydrocarbon phases, and a cubic-plus-association (CPA) EOS for the aqueous phase [40]. The CPA-EOS takes into account the self-association of water molecules, and cross-association between water and CO_2 molecules [49] From molar phase densities, the phase saturations are calculated.

2.5 Three-phase relative permeabilities

We use the Stone model [50, 51] for three-phase relative permeabilities. The details of our implementation are discussed in [40].

2.6 Initial and boundary conditions

With respect to cz_i, Eq. 1 is the first degree, which requires boundary conditions (BC) for molar density and mole fractions at the inflow boundary; the outflow boundary is part of the solution and will be computed. We also need initial conditions for molar density and mole fractions of all components in the domain. With respect to p the pressure Eq. 11 is the first degree. Therefore one either needs pressure as Dirichlet BC for each boundary point of the domain or, since the pressure equation is coupled to Darcy's equation (4) one may provide the normal component of total velocity as Neumann BC for all boundary points. The initial pressure is also required in the domain. The no-flux condition on the impermeable walls for Darcy's equation (4) is implemented simply by setting the permeability $\underline{K}$ to zero on boundary faces.

3 Numerical implementation

Mikyska and Firoozabadi [33] present detailed numerical implementation of the MHFE-DG method for 2D compositional modeling of two-phase flow. Moortgat et al. [46] extend the formulation to three-phase flow in 2D. We present the numerical scheme for 3D three-phase compositional flow in this paper.

The set of Eqs. 1, 9 and 11 along with the thermodynamic equilibrium relations, can be solved for pressure, phase velocities and compositions using an IMPEC scheme. The mixed hybrid finite element (MHFE) method of the lowest order is applied to the pressure field, which is usually smooth and continuous. Fluid properties, on the other hand, show sharp discontinuities, for instance around the front, which are smeared out by numerical dispersion. Therefore a trilinear discontinuous Galerkin (DG) method is implemented for the transport equation which is theoretically first order in space and zero order in time (using forward Euler). Advantages of this combination have been discussed by Hoteit and Firoozabadi [52]. They show that changing the order of the mass transport equation has a significant effect on the accuracy and CPU efficiency of the simulations.

In compositional modeling there are advantages in the use of IMPEC methods. The fundamental assumption of IMPEC is that pressure and concentration equations can be decoupled when the time scale variation of the concentration field is significantly smaller than the variation of the pressure field. Compared with the fully implicit methods, IMPEC methods have smaller and computationally cheaper linear systems. The other advantage of IMPEC methods is the straightforward incorporation of phase stability analyses. The stability analysis identifies whether a fluid phase is stable, and if not, provides an initial guess for the flash computation. Alternatively, phase compositions of the previous time step may provide a good initial guess for flash calculation.

A scalar quantity $c(\mathbf{x}, t)$ in a 3D cubic element K can be represented by four degrees of freedom (DOF), $l = 1,2,3,4$, as

$$c_K(\mathbf{x}, t) = \sum_{l=1}^{4} c_{K,l}(t)\varphi_{K,l}(\mathbf{x}) \quad \mathbf{x} = (x, y, z). \tag{12}$$

where $\phi_{K,l}(\mathbf{x})$ are listed in Appendix A.

Similarly, a generic vector quantity $\mathbf{q}(\mathbf{x}t)$ in an element K can be discretized as:

$$\mathbf{q}_K(\mathbf{x}, t) = \sum_{E \in \partial K} q_{K,E}(t)\mathbf{w}_{K,E}(\mathbf{x}) \quad \mathbf{x} = (x, y, z) \tag{13}$$

where $\mathbf{w}_{K,E}(\mathbf{x})$ is the lowest-order Raviart–Thomas linear basis vector of face Ein an element K listed in Appendix A.

Using this representation, one can write $q_{K,E}$ in Eq. 13 as

$$q_{K,E} = \int_E \mathbf{q} \cdot \mathbf{n}_{K,E} \tag{14}$$

which is the normal component of a vector $\mathbf{q}$ on edge E of an element K with respect to the outer normal $\mathbf{n}_{K,E}$. This form will be used in the derivation of discretized equations.

3.1 MHFE discretization of Darcy's equation

We multiply Darcy's equation (9) by the basis vector field $\mathbf{w}_{K,E}$ and integrate the pressure gradient by parts over element K to find the discretized total velocity:

$$v_{K,E} = a_{K,E}p_K - \sum_{E' \in \partial K} b_{K,E,E'}p_{K,E'} + d_{K,E} \tag{15}$$

Author's personal copy

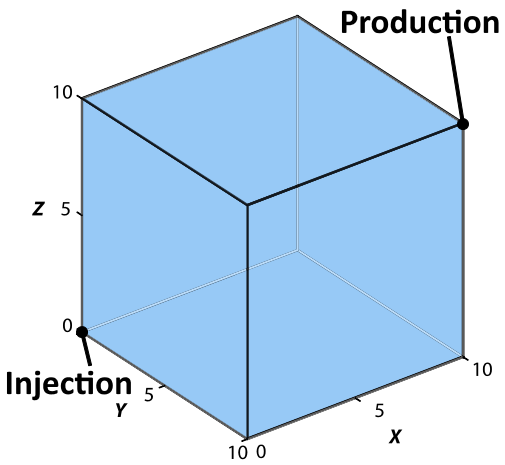

Fig. 1 Schematic of the problem domain (examples 1, 2, and 4)

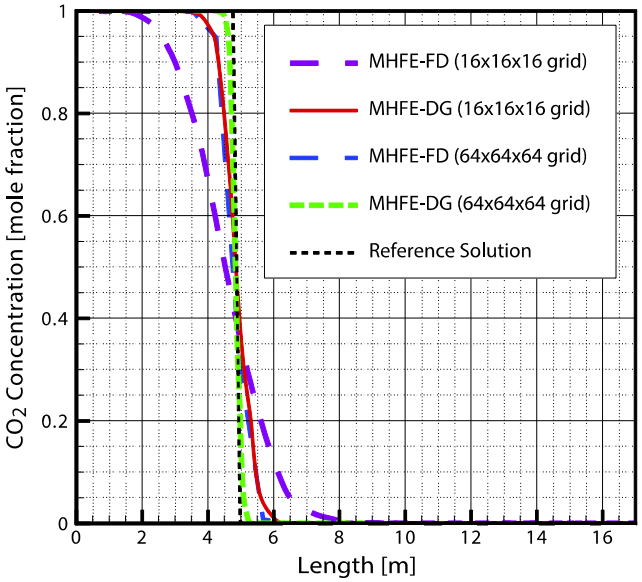

Fig. 2 CO_2 concentration at PVI = 7 %, along a line from injection to production well with MHFE-FD and MHFE-DG methods in 16 × 16 × 16 and 64 × 64 × 64 grids and the reference solution (example 1)

in terms of element-average pressures p_K and face-average pressures $p_{K,E'}$. The coefficients in Eq. 15 are listed in Appendix B.

From flux continuity across face E, the flux can be eliminated by collecting the Darcy velocity and a global matrix system for $\mathbf{p}$ (element-average pressures, p_K) and $\mathbf{p_f}$ (face-average pressures, $p_{K,E}$) can be constructed:

$$\mathbf{R^T p} - \mathbf{M}\,\mathbf{p_f} = \mathbf{V} \tag{16}$$

where $\mathbf{R}$, $\mathbf{M}$ and $\mathbf{V}$ are defined in Appendix B.

3.2 MHFE discretization of pressure equation

The other N_K equations, required for the closure of the pressure system, are from the discretization of the pressure equation (11). The pressure equation is multiplied by basis vector field $\mathbf{w}_{K,E}$ and integrated over each element K. From the continuity of pressures across face E, we can construct a second global matrix system of equations:

$$\mathbf{D}\mathbf{p}^{n+1} - \tilde{\mathbf{R}}\mathbf{p}_\mathbf{f}^{n+1} = \mathbf{G} \tag{17}$$

where superscript n refers to the current time step and $n+1$ to the next time step. Coefficients are listed in Appendix B.

Equation 17 provides N_K equations, which, along with equation (16) give a closed system with $N_K + N_E$ equations and $N_K + N_E$ unknowns. The matrix $\mathbf{D}$ is diagonal, so we can eliminate $\mathbf{p}$ to find:

$$\left(\mathbf{M} - \mathbf{R^T D^{-1}}\tilde{\mathbf{R}}\right)\,\mathbf{p}_\mathbf{f}^{n+1} = \mathbf{R^T D^{-1} G} - \mathbf{V}. \tag{18}$$

Once $\mathbf{p}_\mathbf{f}^{n+1}$ is calculated, the cell-averaged pressure $\mathbf{p}$ can be updated from Eq. 17 and the total velocity from Eq. 15. Then phase velocity is calculated from Eq. 10 as discussed in Appendix C.

3.3 DG discretization of molar balance equations

We use the discontinuous Galerkin scheme to discretize the component transport Eq. 1. This equation is written in the weak form by multiplying test function $\varphi_{K,l}$ and integrating over each element K. The time derivative is approximated

Table 1 Gridding in example 1

Grid cells	Number of grid cells	Number of edges	Number of nodes	Size of 3D linear system	Size of (corresponding) 2D linear system
4 × 4 × 4	64	240	125	237	38
8 × 8 × 8	512	1728	729	1725	142
16 × 16 × 16	4096	13,056	4913	13,053	542
32 × 32 × 32	32,768	101,376	35,937	101,373	2110
64 × 64 × 64	262,144	798,720	274,625	798,717	8318

Author's personal copy

Table 2 CPU time (minutes) for different grids at PVI = 7 % (example 1)

Number of grid cells	64	512	4096	262,144
CPU time, MHFE-DG	<1 s	0.067	1.36	3078.6
CPU time, MHFE-FD	<1 s	0.057	1.29	3066.6

by the forward Euler method. The final form of the DG discretized mass balance equation reads

$$\phi_K \sum_{j=1}^{4} \frac{c_K z_{i,K}^{j\ n+1} - c_K z_{i,K}^{ln}}{\Delta t} M_{j,l}^K - \sum_{\alpha} \sum_{j=1}^{4} c_{\alpha,K} x_{\alpha i,K}^j \sum_E v_{\alpha,K,E} M_{j,l}^{K,E} + \sum_E \sum_{\alpha} \frac{\tilde{c}_{\alpha,K} \tilde{x}_{\alpha i,K,E} v_{\alpha,K,E}}{|E|} M_l^E + \sum_E |E| J_{\alpha i,K,E} M_l^E = \int_K F_{i,K} \varphi_{K,l} \tag{19}$$

in terms of the element averaged phase compositions $x_{\alpha i,K}$ and six upwind phase compositions $\tilde{x}_{\alpha i,K,E}$ for the six faces. Different integral coefficients $\mathbf{M}$ are listed in Appendix B. The quantities $\tilde{x}_{\alpha i,K,E}$ and $\tilde{c}_{\alpha,K,E}$ are the composition (mole fraction) of component i and phase α density on edge E of element K. The face values are upwinded depending on the velocity direction. On the edge common between two elements K and K':

$$\tilde{x}_{\alpha i,K,E} = \begin{cases} x_{\alpha i,K,E} & \text{if } v_{\alpha,K,E} \geq 0 \\ x_{\alpha i,K',E} & \text{if } v_{\alpha,K,E} < 0 \end{cases} \tag{20}$$

$$\tilde{c}_{\alpha,K,E} = \begin{cases} c_{\alpha,K,E} & \text{if } v_{\alpha,K,E} \geq 0 \\ c_{\alpha,K',E} & \text{if } v_{\alpha,K,E} < 0. \end{cases} \tag{21}$$

These values are calculated by the flash procedure described in Section 2.4. A maximum of seven flash calculations are performed for each element at each time step for the DG method in 3D

In Eq. 19 $J_{\alpha i,K,E} = \mathbf{J}_{\alpha,i,K}.\mathbf{n}_{K,E}$ is the average diffusive flux through edge E which is assumed continuous across edges. By considering the diffusion flux term only when $l = 1$, it is treated with finite difference scheme. But due to the secondorder spatial variation in diffusion, the term is quadratic in Δx. Higher-order discretization of the multicomponent diffusion flux is beyond the scope of this work [41].

It is well known that higher-order methods may exhibit spurious oscillations, unless a slope limiting procedure is adopted. We use the same slope limiter as in earlier works [33, 53], which is discussed in Appendix D. An itemized description of the full algorithm and corresponding flowchart are provided in Appendix E.

4 Numerical examples

In order to demonstrate the superiority of the higher-order methods for transport equation in both lab and field scales and to examine the effect of dimensionality (2D versus 3D), we start with a few simple examples illustrating the efficiency of the proposed algorithm in terms of CPU time and convergence rate and then we will consider challenging 3D compositional multicomponent multiphase fingering simulation in examples 5 to 7.

Examples 1 to 5 are performed on a 3.1GHz Intel Core i5 Macintosh machine, and examples 6 and 7 on a 2.8GHz Intel Core i7. We note that all CPU times are conservative and based on strict adherence to the CFL time constraint, which is sufficient but not necessary for numerical stability (for less complicated flow, we can use a more relaxed time-constraint, based on the maximum *net* number of moles in a grid cell in one time-step). All simulations are carried out in serial mode, but the code is parallelized for shared-memory architectures. The phase-split computations, in particular, scale well with the number of cores available. This makes the higher-order DG method even more competitive with respect to the traditional FD approach, because the main extra cost of the higher-order DG method is additional flash computations (seven flash calculations for each 3D element rather than one per element in FD), which are trivially

Table 3 Relevant data for the initial oil phase (example 2)

Component	Initial oil composition [mole fraction]	Acentric factor (ω) [−]	Critical temperature (T_c) [K]	Critical pressure (p_c) [bar]	Molar weight (M_w) [g/mol]	Critical specific vol (V_c) [cm^3/g]	Volume shift (s) [−]
C_1	0.4499	0.0110	190.56	45.99	16.00	0.00615	−0.1540
C_2–C_3	0.1220	0.1178	327.81	46.54	34.98	0.00474	−0.0949
C_4–C_5	0.0513	0.2103	435.62	36.09	62.98	0.00437	−0.0598
C_6–C_{10}	0.1345	0.4175	574.42	25.04	116.19	0.00425	0.0466
C_{11}–C_{24}	0.1677	0.6632	708.95	15.02	218.76	0.00410	0.1494
C_{25+}	0.0745	1.7276	891.47	7.47	465.91	0.00350	0.4950

Author's personal copy

Table 4 Relevant data for water and CO_2 (example 2)

	Acentric factor [−]	Critical temperature (T_c) [K]	Critical pressure (p_c) [bar]	Molar weight (M_w) [g/mol]	Critical specific vol (V_c) [cm^3/g]	Volume shift (s) [−]
H_2O	0.344	647.29	220.90	18.02	–	Li and Firoozabadi [49]
CO_2	0.239	304.14	73.75	44.00	0.00214	−0.1768

parallelized. A fully parallelized version for distributed-memory cluster environments is in the works.

In this work, FD and DG only refer to the mass transport update. In both methods, the pressure and velocity fields are computed using the same MHFE method,x designated as MHFE-FD and MHFE-DG. As a result, the degree of numerical dispersion observed in the FD simulations is conservative.

4.1 Example 1: single-phase CO_2 injection in a C_1-saturated 3D homogeneous domain

In this example, CO_2 is injected in a 10 m × 10 m × 10 m 3D domain at a constant rate of 10 PV/year from a well located at the corner (0 m, 0 m, 0 m). The production well produces at a fixed pressure of 300 bar at the diagonally opposite corner at (10 m, 10 m, 10 m), as depicted in Fig. 1. The initial pressure at the bottom of domain is 300 bar and the temperature is 450 K. The permeability is 10 md and the porosity is 20 %. The domain is saturated with C_1 and there is no phase change. The CO_2 front and numerical dispersion will be compared for the two methods (MHFE-DG versus MHFE-FD).

Five different grids listed in Table 1 are used. This table provides the number of elements (that is, grid cells), edges and nodes of the grids. The size of the linear systems to be solved is also provided in both 3D and 2D.

Since the fluid is in single-phase, we expect a sharp front of CO_2 propagating through the domain. The CO_2 concentration profile along the line connecting the injection and production wells provides a measure of numerical dispersion for each method. Figure 2 depicts the CO_2 concentration along the cube-diagonal line at PVI = 7 % with different discretization schemes and grid sizes. We expect a stepwise reference solution, which is shown along with the result from MHFE-DG and MHFE-FD methods in 16 × 16 × 16 and 64 × 64 × 64 grids in Fig. 2. As the figure shows, the MHFE-DG method in a 16 × 16 × 16 grid has the same numerical dispersion as the MHFE-FD method in a 64 × 64 × 64 grid.

Table 2 compares the CPU times of the simulations for both methods, which demonstrates that for the same order of accuracy, MHFE-DG is more than three orders of magnitude faster than MHFE-FD considering that no flash calculation is carried out for this example.

Table 5 Relative permeability (example 2)

S_{wr}	0.1	k^0_{row}	0.69
S_{gr}	0.02	k^0_{rog}	0.95
S_{orw}	0.4	n_w	3
S_{org}	0.1	n_g	2
k^0_{rw}	0.4	n_{ow}	2
k^0_{rg}	0.63	n_{og}	2

4.2 Example 2: convergence analysis for three-phase multi-component flow in a 3D homogeneous domain

We consider a water-flooded domain and inject CO_2 in the same configuration as depicted in Fig. 1 The initial pressure, temperature, permeability, and porosity are also the same as in example 1. This is an eight-component, three-phase problem.

Fluid data for oil, water and CO_2 are given in Tables 3 and 4. The domain has an initial water saturation of 40 %; relative permeability parameters are given in Table 5.

The overall accuracy is computed in terms of the L_1 norm, which is the average absolute value of the difference between the reference and the numerical solution. The rate of convergence of the MHFE-FD and MHFE-DG methods is compared in Table 6 and Fig. 3, based on the results of simulations in different grids in Table 1.

The reference solution is estimated based on a sequence of three solutions (8, 16 and 32 elements in each direction) using the Richardson extrapolation [54] of the concentration of CO_2 in the domain. As depicted in Fig. 2, the average convergence rates of MHFE-DG and MHFE-FD are 1.140 and 0.573, respectively. Using first-order polynomials ($p = 1$) to approximate the solution in each element, the MHFE-DG method should theoretically have second-order convergence rate ($p + 1 = 2$) for a smooth solution. This case is not a smooth solution in parts of the domain around the front; therefore the convergence rate is less than the theoretical value of 2 [40, 55].

Figure 4 shows CPU times of the MHFE-FD and MHFE-DG methods for the grids in Table 1 versus the L_1 norm, normalized to the MHFE-FD L_1 norm in the coarsest mesh. As an example, for the order of accuracy equal to 0.2,

Author's personal copy

Table 6 Rate of convergence of MHFE-FD and MHFE-DG (example 2)

Number of grid cells	MHFE-FD		MHFE-DG	
	L_1	Rate of convergence	L_1	Rate of convergence
262,144	0.007296		0.001383	
32,768	0.011108	0.606442	0.003238	1.226801
4096	0.016666	0.585266	0.007147	1.142275
512	0.024702	0.567781	0.015125	1.081447
64	0.035743	0.533015	0.032673	1.111184

MHFE-FD requires more than three orders of magnitude CPU time than MHFE-DG.

4.3 Example 3: single-phase C_1 injection in a heterogeneous 3D domain saturated with C_3

We consider the 3D heterogeneous 10 m × 10 m × 10 m domain shown in Fig. 5 which has a near impermeable zone ($\underline{K} = 10^{-7}$ md) in one part, while the rest of the domain has a permeability of 10 md. The domain is initially saturated with propane (C_3). Methane (C_1) is injected at a low rate of 0.1 PV/year at (0 m, 0 m, 0 m) to displace C_3 to the opposite producing corner at (10 m, 10 m, 10 m). The initial pressure at the bottom of domain is 20 bar and the temperature is 394 K. At the condition of this problem, the C_1–C_3 mixture remains in single-phase.

The results are computed with the MHFE-DG method and MHFE-FD method in both 20 × 20 × 20 grid and 40 × 40 × 40 grid. MHFE-DG results in a finer grid of 40 × 40 × 40 (not shown) are not significantly different than the coarser results; the MHFE-DG solution has already converged on the 20 × 20 × 20 grid. Figure 6 shows methane composition at one PVI. The MHFE-DG and MHFE-FD results are very different, with significant numerical dispersion from the MHFE-FD method, even in a finer 40 × 40 × 40 grid at a significantly higher CPU time, as shown in Fig. 6c and Table 7.

4.4 Example 4: comparison between 2D and 3D simulations

In this example we compare simulation results in 2D and 3D to illustrate differences in the flow pattern and breakthrough time. We consider the same single-phase problem as in example 1 for CO_2 injection into methanesaturated media, but we use a perforated injection well at (0 m, 0 m, 0 m < z < 10 m) and a perforated production well at (10 m, 10 m, 0 m < z < 10 m). The initial pressure is 300 bar at the bottom of the domain with an established pressure profile along vertical direction that satisfies hydrostatic equilibrium. The initial and subsequently fixed pressure at the producer will therefore be lower in the top than in the bottom. For the 2D simulation, we take a diagonal 14.14 m × 10 m vertical cross-section from the injection to the production well.

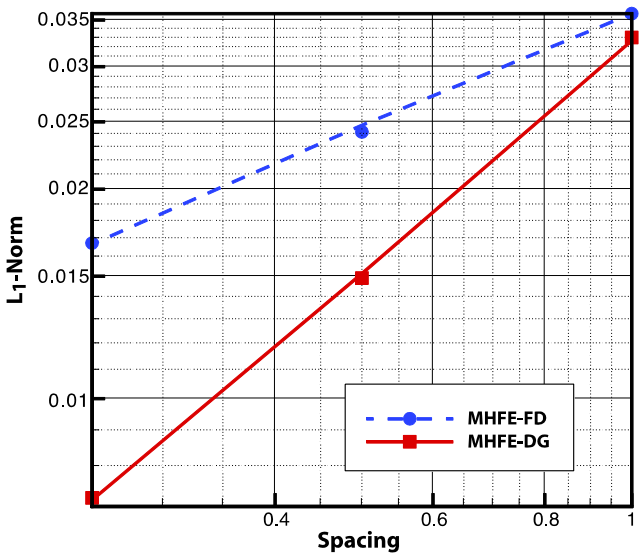

Fig. 3 L_1-norm (logarithmic scale) versus spacing (logarithmic scale) for MHFE-DG and MHFE-FD schemes 864 (example 2)

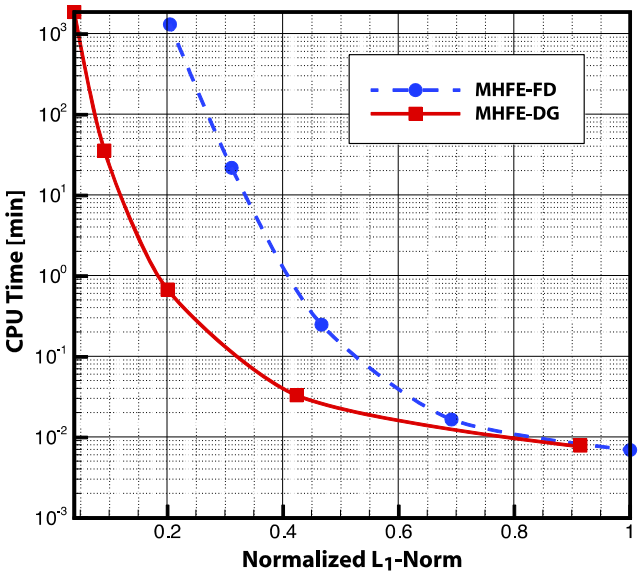

Fig. 4 CPU time (logarithmic scale) versus L_1-norm for the MHFE-DG and MHFE-FD schemes (example 2)

Author's personal copy

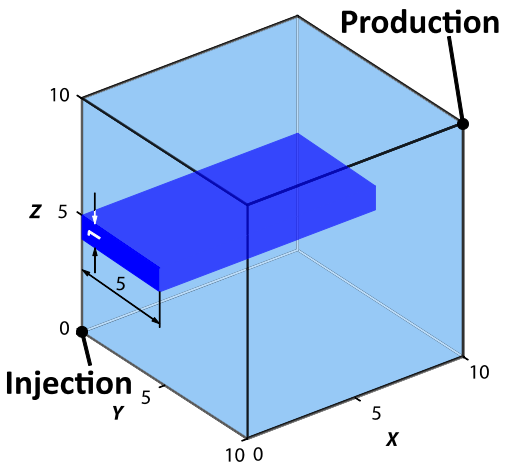

Fig. 5 Schematic of domain (example 3)

MHFE-DG simulations are carried out in a 32 × 32 (× 32) grid in 2D (3D). Figure 7 compares a diagonal cross-section of the 3D simulation (a) to the 2D result (b).

As expected, the 3D result shows more numerical dispersion. Numerical dispersion is particularly challenging in 3D, which may be the reason that few 3D studies of compositional gravity fingering are reported in the literature. The 3D simulation predicts about 25 % PVI earlier breakthrough time than the 2D simulation as shown in Fig. 8. Part of discrepancy could be attributed to higher numerical dispersion in the 3D simulation and could be resolved numerically by e.g. using finer mesh, but it is in part related to the flow pattern and the way it is affected by the other boundary conditions in the 3D domain, which do not exist in 2D and could not be simulated correctly even for such a simple geometry.

4.5 Example 5: gravitational fingering during CO_2 injection into a vertical core

In this example we model gravitational fingering at the core scale. There are two main objectives: to examine the applicability of 2D simulation for 3D processes, and to demonstrate that the FD method may not adequately represent complex fingering patterns even at the laboratory scale.

Table 7 CPU time (min) for different number of cells at PVI = 100 % (example 3)

Number of grid cells	800	64,000
CPU time, MHFE-DG	100	–
CPU time, MHFE-FD	93	4585

We use the data from a series of core flooding experiments [56]. We convert a cylindrical core to a 3.9 cm × 3.9 cm × 27.3 cm domain, in which CO_2 is injected from the top at a rate of one hydrocarbon PV per day. The connate water saturation is 31 %, and all other residual saturations are assumed equal to zero. The end-point water relative permeability is one, the end-point gas relative permeability is 0.6, the end-point oil relative permeability to water is 0.3, and the end-point oil relative permeability to gas is 0.4. All the Corey exponents are one (linear). The absolute permeability of the sandstone core is 221 md and the porosity is 19 %. The temperature is 331.2 K and the initial pressure is 441.3 bar at the bottom of core, which is kept constant during the experiment. The fluid properties and initial oil composition are provided in [56]. The density of CO_2 is 0.92 g/cm^3 and the oil density is 0.74 g/cm^3 at the initial conditions of the core. Because CO_2 is denser than the oil at this condition, the fluid system is unstable and we expect gravitational fingers to form during injection from the top. Dampening effects of Fickian diffusion, capillary forces and layering in similar problems on the development of instabilities and on the onset of fingering and total recovery are discussed in [56, 57] and [58].

Figure 9 compares oil recovery for all the simulations in this example. MHFE-DG simulation results in 18 × 18 × 80 and 25 × 25 × 100 element grids show excellent agreement with the experimental data and near convergence in the 18 × 18 × 80 grid. Figure 10 shows simulation results for CO_2 concentration profiles from MHFE-FD and MHFE-DG at PVI = 10, 20 and 60 %. As expected, the lower-order MHFE-FD method in the same grid produces very different results. Numerical dispersion causes significant dampening of the instabilities, which, as shown in Fig. 10c, develop at much later time (PVI = 60 %). Consequently, the

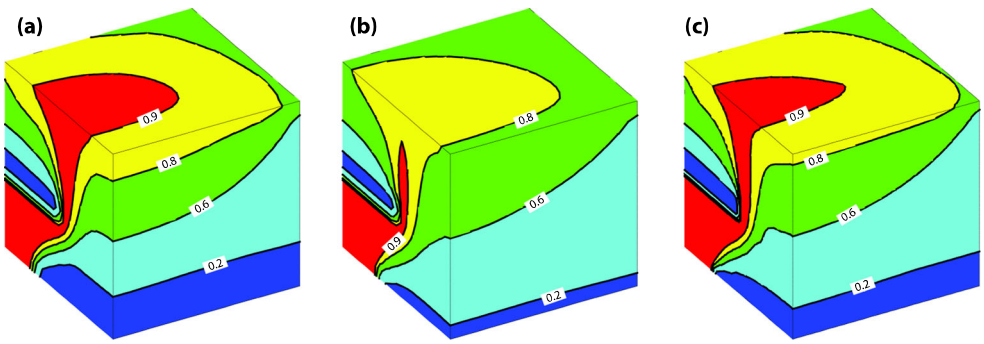

Fig. 6 Methane composition profile (mole fraction) at PVI = 100 % by **a** MHFE-DG in a 20 × 20 × 20 grid, **b** 869 MHFE-FD in a 20 × 20 × 20 grid, and **c** MHFE-FD in a 40 × 40 × 40 grid (example 3)

Author's personal copy

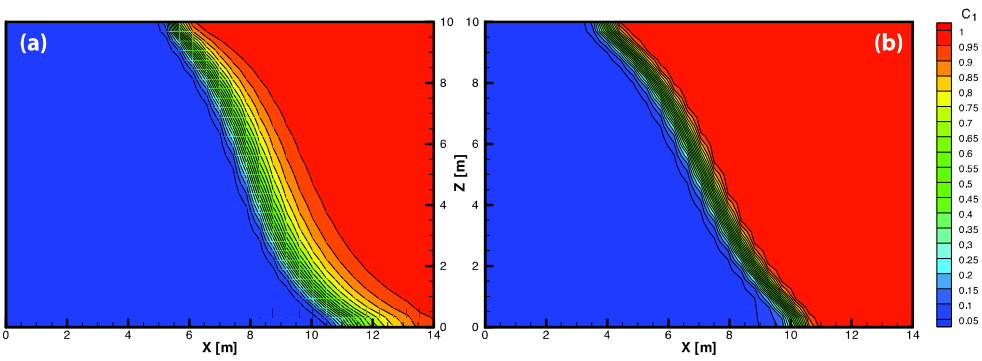

Fig. 7 Methane concentration at PVI = 50 % **a** in 3D and **b** in 2D simulations both using MHFE-DG (example 4)

gravitational fingers are suppressed in the MHFE-FD simulation, and we observe piston-like displacement. The MHFE-FD simulation significantly over-predicts the final oil recovery (Fig. 9).

In the numerical simulation, the instability and onset of fingering is triggered by truncation errors. ....Moortgat et al. [56] mention the dimensionality issue as one probable source of discrepancy between 2D simulation results and experimental data. Figure 11 compares 2D and 3D results at three different times (PVI = 15 %, the onset of instability in 3D simulation; PVI = 23 %, the onset of instability in 2D simulation, and PVI = 50 %). The 3D results are from the mid-plane. Instabilities are more pronounced in 3D, which results in the earlier onset of fingering (15 % PVI in 3D versus 23 % PVI in 2D), and consequently earlier breakthrough time, as depicted in Fig. 11c. The average speed of the fingers in 3D is 6.64 μm/s which is about 11.5 % higher than 5.95 μm/s in 2D. Figure 9 shows that the 3D simulations are indeed in closer agreement with the experimental data than the 2D simplification despite the likely higher numerical dispersion in 3D.

4.6 Example 6: field-scale CO_2 injection with gravitational fingering in 2D and 3D

The focus of this example is on the simulation of largescale fingering. We investigate the effect of density increase from CO_2 dissolution in the oil phase and the associated phase behavior in 3D. There is no reported investigation in the literature in 3D for this problem. In CO_2 injection from the top, even when the injected CO_2 is lighter than the oil phase, gravity drainage may be unstable, as has been recently discussed by Ahmed et al. [59] in 2D. The layer of denser oil on top of lighter oil may trigger fast gravito-convective mixing, particularly when the permeability is high. A similar effect (considered in the next example) plays a central role in CO_2 sequestration from the top, when CO_2 dissolution increases the water density modestly (up to 1 %). In recent years, densitydriven flows from CO_2 injection has been discussed in the literature [10, 37]. In this example, we will show

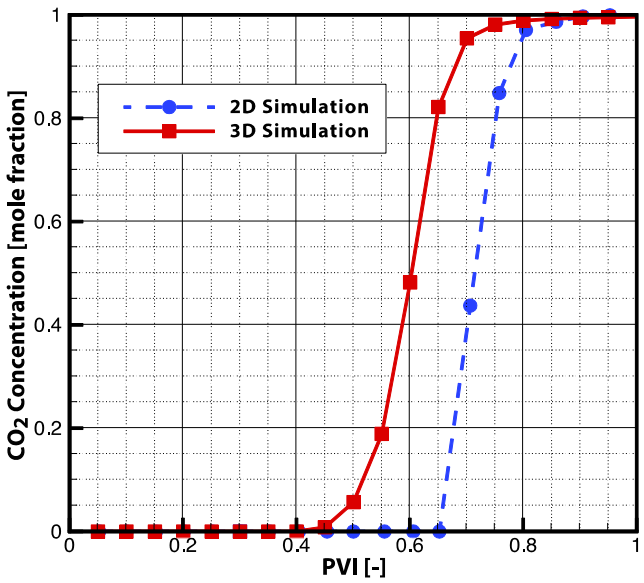

Fig. 8 CO_2 concentration at the bottom of the production well from 2D and 3D simulations (example 4)

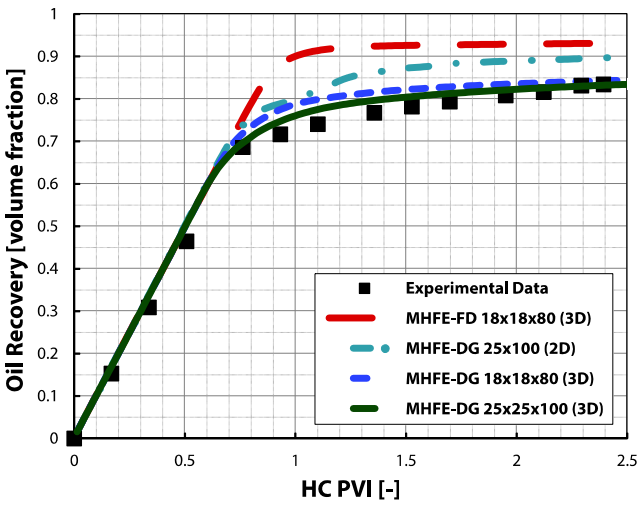

Fig. 9 Oil recovery as a function of hydrocarbon PVI for different grids with MHFE-DG and MHFE-FD in 3D and 2D (example 5)

Author's personal copy

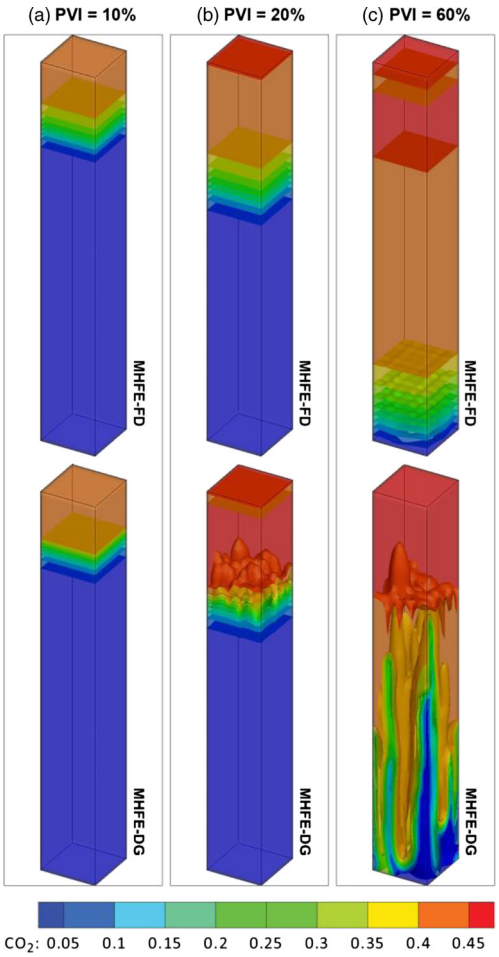

Fig. 10 Overall CO_2 concentration (mole fraction) at **a** PVI = 10 %, **b** PVI = 20 %, and **c** PVI = 60 % from MHFE-FD and MHFE-DG simulations in 18 × 18 × 80 grid (example 5)

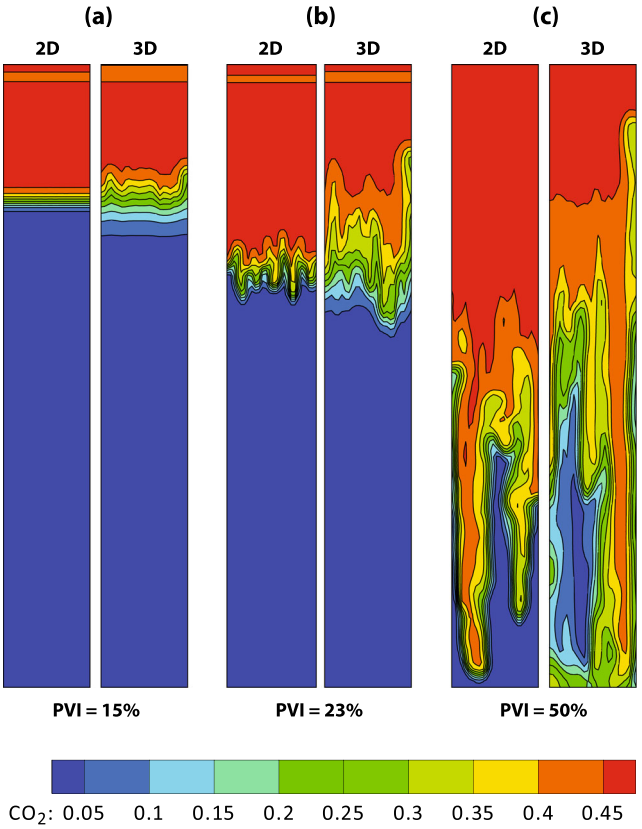

Fig. 11 Overall CO_2 concentration at PVI = 15 % (**a**), 23 % (**b**), and 50 % (**c**) for 2D and 3D MHFE-DG in (25 ×) 25 × 100 grids. 3D results are from mid-plane of the core (example 5)

that our higher-order scheme is a powerful tool to simulate fingering in 3D where finite difference codes have inherent limitations.

Ahmed et al. [59] pose, correctly, that slim tube experimental data represent 1D horizontal flow and cannot be generalized for field evaluation purposes. Particularly when fingering occurs, the flow cannot be represented in 1D, and may not even be captured fully in 2D. Ahmed et al. [59] perform field-scale simulations in 2D with the CMG commercial simulator, which is based on the traditional FD method. In this example, we first present 2D results with our MHFE-FD method and compare to higher-order MHFE-DG results. More importantly, we generalize to fine-grid 3D simulations, showing density-driven flow and fingering in compositional 3D flow. We also consider the effect of Fickian diffusion, which may act as a restoring force in fingering instabilities.

We consider a domain that is about half the size of that in [59] to make the 3D simulations numerically tractable. The 3D domain is 200 m × 50 m × 50 m, and 200 m × 50 m for the 2D simulations. We carry out simulations in 160 × 40 × 40, 140 × 35 (× 35), 100 × 25 (× 25), and 80 × 20 (× 20) grids in 2D (3D). To further test convergence, we also use finer 400 × 100, 300 × 50, and 200 × 50 grids in 2D.

The domain has a 1 darcy permeability and 22 % porosity. The initial bottom hole pressure is 117 bar and the temperature is 320 K. Residual saturations are assumed equal to zero, all endpoint relative permeabilities are one with quadratic Corey exponents. The fluid properties and initial oil composition are provided in [59] At the given condition, pure CO_2 has a density of 0.618 g/cm^3 and viscosity of 0.02 cp. We note that our phase behavior predictions for the oil–CO_2 mixtures do not agree well with those reported in [59]. We find a higher CO_2 solubility of about 70 mol% and initial density and viscosity of 0.741 g/cm^3 and 0.46 cp, respectively. The density and viscosity of the oil fully saturated with CO_2 at the given temperature and pressure

Author's personal copy

are 0.778 g/cm^3 and 0.19 cp, respectively. Despite these differences, we observe a similar density increase of 5 % from CO_2 dissolution, which is the focus of this example.

As in [59] for 2D, CO_2 is injected from the top-left corner at a constant rate of 0.05 PV/year, and production is at a constant pressure from the bottom-right corner. When the 3D reality is simulated with a 2D model, the assumption is that the flow is invariant in the third direction. For the 3D simulations, in order to be comparable to 2D results, we inject uniformly from all elements along the top-left y-axis (0 m, 0 m $< y <$ 50 m, 50 m) at the same rate. Production is from the bottom-right y-axis (200 m, 0 m $< y <$ 50 m, 0 m).

Figure 12 presents the results at 10 % PVI from 2D simulation in five different grid sizes using the MHFE-FD and the higher-order MHFE-DG methods. Fickian diffusion is first neglected for comparison to results in [59]. Because we use the same injection rate of 0.05 PV/year as in [59], but about half the domain size, the effective rate is about twice as low (the front moves at half the speed). As a result, we see in the MHFE-FD results that there is more time for gravitational downward flow. Compared to the MHFE-

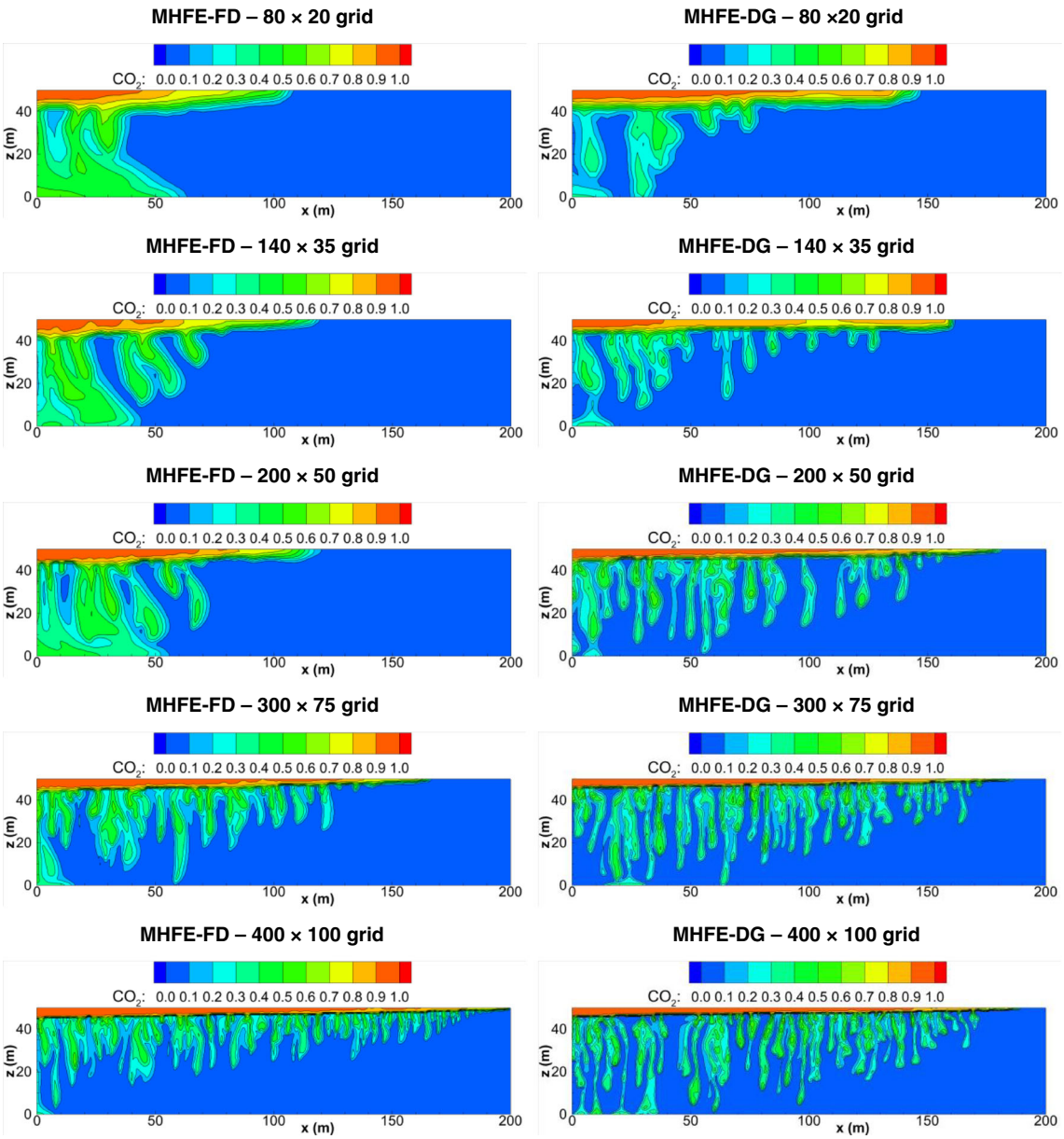

Fig. 12 Overall CO_2 concentration (mole fraction) at 10 % PVI from MHFE-FD and MHFE-DG in five different grid 880 sizes, without Fickian diffusion (example 6)

Author's personal copy

Table 8 CPU times for MHFE-FD and MHFE-DG in different grids (example 6)

Grid cells	MHFE-FD (h:min:s)	MHFE-DG (h:min:s)
2D: 80 × 20 without diffusion	00:00:16	00:00:36
2D: 140 × 35 without diffusion	00:01:34	00:03:38
2D: 140 × 35 with diffusion	00:02:32	00:04:42
2D: 200 × 50 without diffusion	00:05:12	00:11:30
2D: 200 × 50 with diffusion	00:07:34	00:13:59
2D: 300 × 75 without diffusion	00:25:03	00:38:29
2D: 400 × 100 without diffusion	01:15:27	01:35:59
3D: 80 × 20 × 20 without diffusion	00:18:00	00:35:00
3D: 100 × 25 × 25 without diffusion	01:08:00	02:18:00
3D: 140 × 35 × 35 without diffusion	15:28:00	17:25:00
3D: 160 × 40 × 40 without diffusion	34:58:00	40:35:00

DG simulations, it is clear that the numerical dispersion in the FD simulations is pronounced, which suppresses the formation of gravitational fingers unless extremely fine grids are used. In the coarsest grids, which are far finer than what is generally used for large field-scale simulations, the fingering is not resolved at all and the location of front, which determines the breakthrough time, is severely underestimated (100 m on the coarsest grid, versus200 m on the finest).

Conversely, the DG results quickly converge in terms of the location of the front in the top and the finger penetration depth, with smaller scale details being resolved in the finest grids. Without performing another convergence analysis as considered in example 2, it is apparent that the DG results converge at a higher rate than the FD simulations. In terms of CPU time, a DG simulation requires about twice the CPU time of a FD simulation in the same grid. This is because the smooth pressure field is calculated with similar CPU times in MHFE-FD and MHFE-DG methods. In the MHFE-DG simulation, there is a DG update step but it causes negligible difference in CPU time compared to MHFE-FD. The significant difference in CPU time is due to the additional flash calculations in 3D MHFE-DG, which is seven instead of one per element and five instead of one in 2D MHFE-FD Implementing different optimization techniques reduce this difference. For example the additional flash computation can only be performed near fronts, or wherever the gradients in compositions are not negligible. Also, the stability and flash calculations can be skipped in many elements where it is possible to determine the state of element as single-phase a priori. It results in about two times more CPU time for MHFE-DG compared with a MHFE-FD simulation on the same grid. In very large grids, such as in 3D, the CPU times become closer, because the linear solver dominates the computational cost. The listed CPU times of this example in Table 8 along with the results shown in Fig. 12 indicate that the FD simulations require five to ten times more CPU in 2D to achieve similar accuracy, due to the lower convergence rate (e.g. 01:15:27 instead of 00:13:59 if MHFE-FD result on 400 × 100 grid is comparable, qualitatively, with MHFE-DG result on 200 × 50 grid). Note that this example relies on a direct solver, which becomes inefficient at very large system sizes.

Fickian diffusion generally acts as a restoring force for viscous and gravitational fingering. Formation of a finger results in relatively steep compositional gradients between the finger and the surrounding oil. Such compositional gradients are smeared out by Fickian diffusion.

Figure 13 shows simulation results at two levels of grid refinement for MHFE-FD and MHFE-DG. We find that

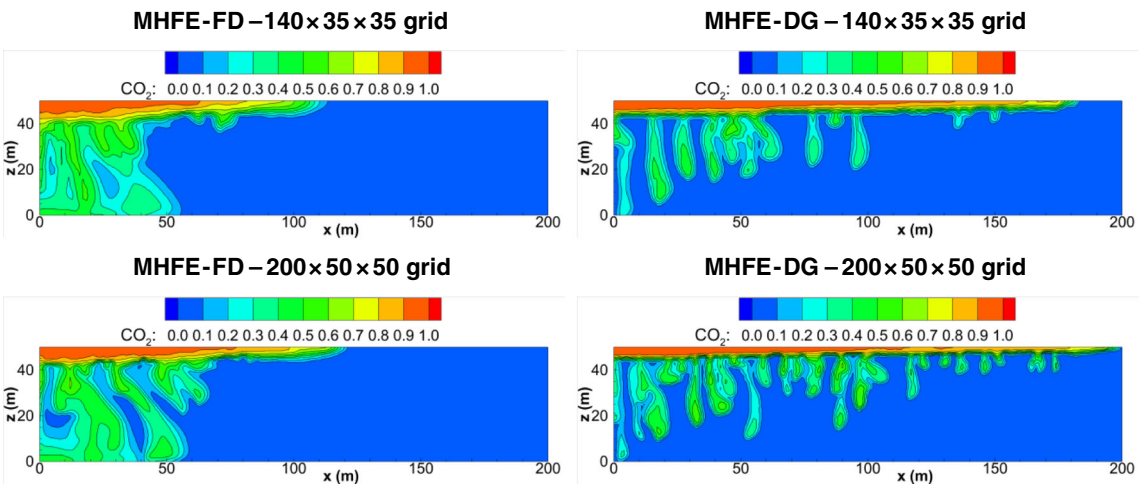

Fig. 13 Overall CO_2 concentration (mole fraction) at 10 % PVI from MHFE-FD and MHFE-DG simulations in two different grid sizes, with Fickian diffusion (example 6)

Author's personal copy

for the large density increase in this problem, with a corresponding pronounced instability, Fickian diffusion is not sufficient to affect the instability appreciably. Diffusion is therefore neglected in the 3D simulations.

Figure 14 shows the results of 3D simulations at 10 % PVI for MHFE-FD and MHFE-DG in four different grid sizes. The viewing angle is from the bottom to clearly illustrate the fingers. Horizontal instabilities and viscous finger formation are also depicted in this figure. Again we see, qualitatively, that the MHFE-FD results are more dispersed and resemble MHFE-DG results in significantly coarser grids. Because the MHFE-FD method converges at about half the rate as the MHFE-DG approach (example 2), the computational cost of obtaining converged results in 3D becomes prohibitive.

Figure 15 compares the overall CO_2 concentration from 2D and 3D MHFE-DG simulations in the 140 × 35 (× 35) grid. The 3D results are from three different cross-sections along the y-direction at $y = 10$ m, $y = 25$ m (midplane) and $y = 40$ m. The onset times of the instability in 2D and 3D are comparable but numerical dispersion is more pronounced in 3D. It should be mentioned that we have not triggered the fingers artificially in this example, which is sometimes done when numerical dispersion would otherwise

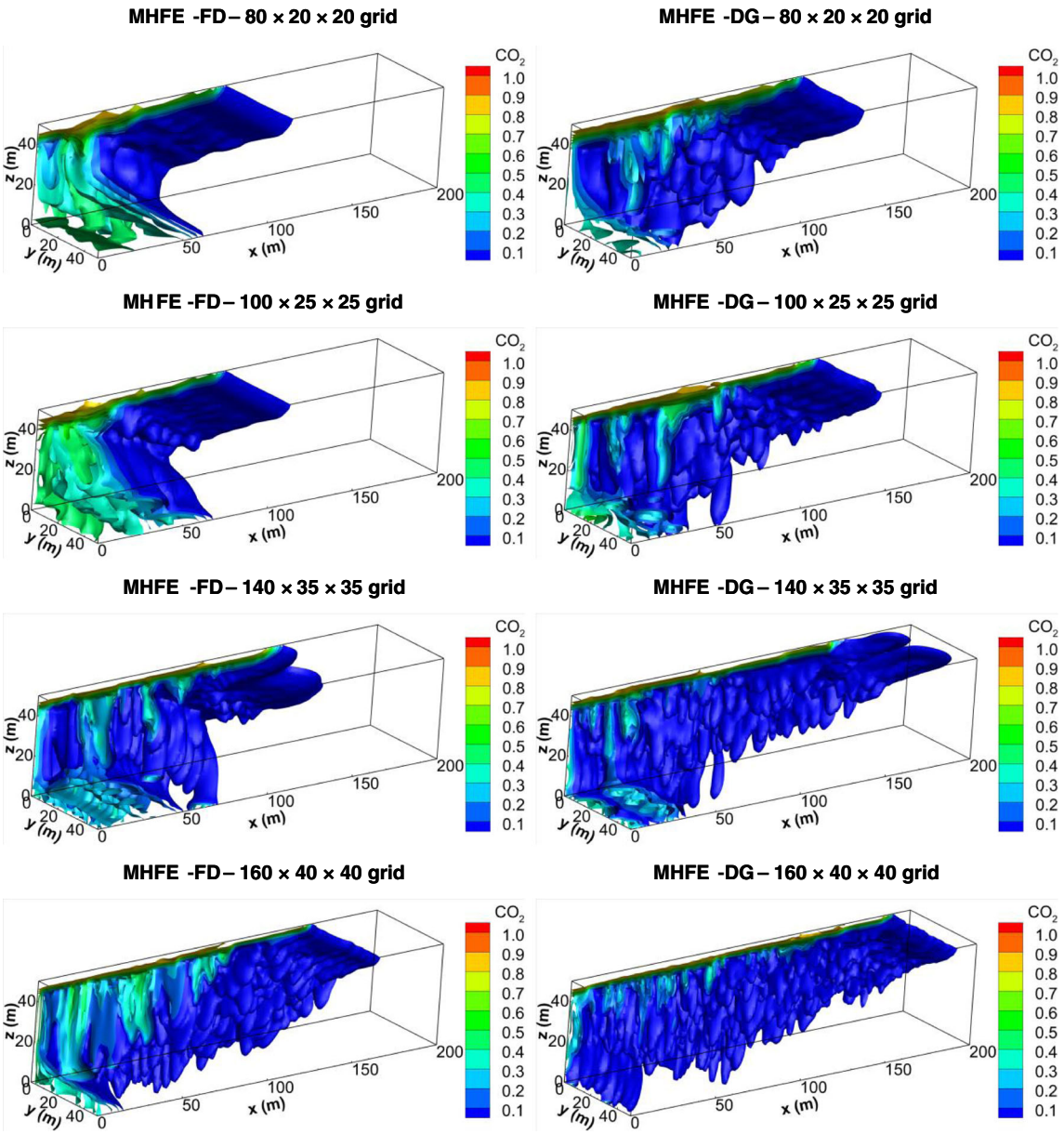

Fig. 14 Overall CO2 concentration (mole fraction) at PVI = 10 % PVI from MHFE-FD and MHFE-DG simulations in four different grid sizes, without Fickian diffusion (example 6)

Author's personal copy

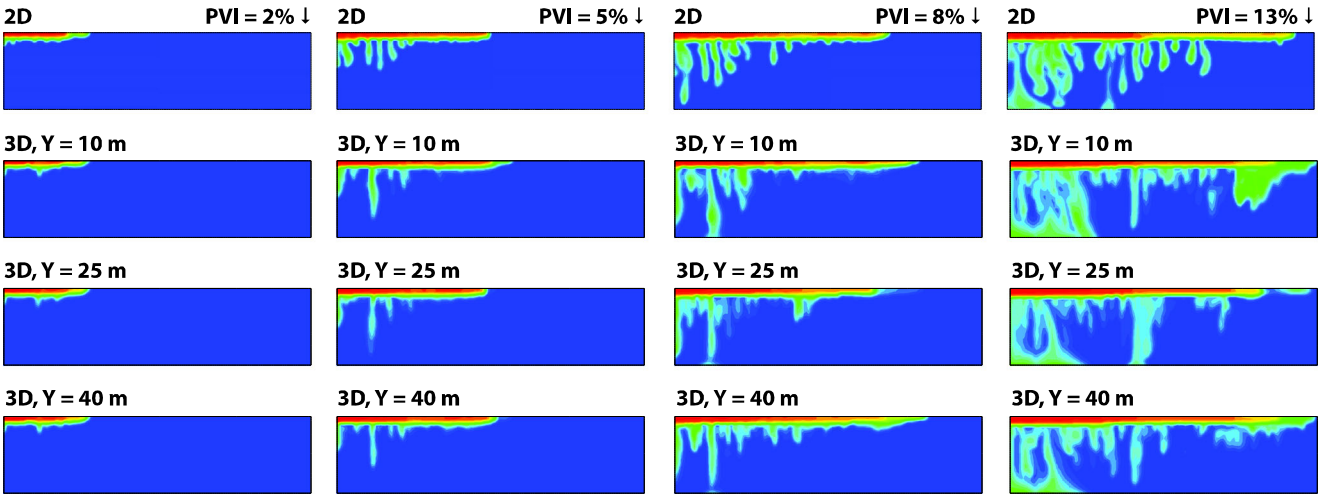

Fig. 15 Comparison between 2D (top row) and 3D results in 140 × 35 (× 35) grid, from different cross-sections 887 along the y-axis (*second row*: $y = 10$ m, *third row*: $y = 25$ m, and *forth row*: $y = 40$ m); results for overall CO_2 concentration at 2, 5, 8, and 13 % PVI (example 6)

suppress the onset of the instability. When a randomly perturbed permeability field is used, the results are similar for this example. Because of the high density increase considered here, the fingers develop readily.

4.7 Example 7: CO_2 sequestration with gravitational fingering in 2D and 3D

In this example we simulate CO_2 sequestration in 3D for a setup similar to that in Pau et al. [10] Specifically, we consider a 8 × 8 × 32 m^3 domain with 0.5 darcy permeability and 15 % porosity. The domain is discretized by a fine 80 × 80 × 80 grid. The grid is linearly refined in the vertical direction, with 20 cm tall cells in the top, where the small-scale onset of fingering takes place, 40 cm in the middle, where fully developed large fingers are expected to propagate, and 2.5-m cells in the very bottom row, where we will not require the same level of accuracy. This grid has 512,000 grid cells, and 1555200 pressure unknowns on grid faces, which is about the upper limit for a serial simulation. As in [10], we consider a 1 % random perturbation around the average permeability in each grid cell (but uniform porosity).

We consider an aquifer temperature and pressure of 350 K and 100 bar, respectively. At these conditions, the pure aqueous phase density is 978 kg/m^3, the maximum

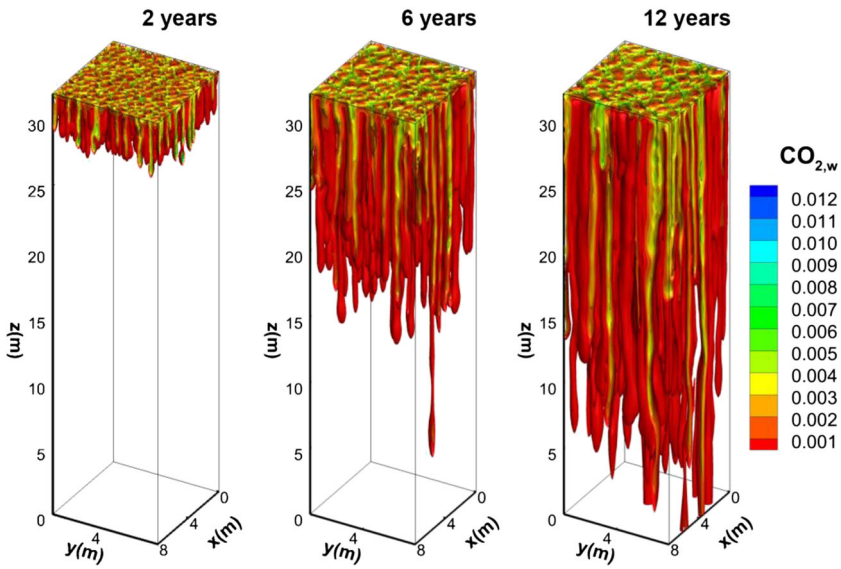

Fig. 16 CO_2 concentration in the aqueous phase (mole fraction) after 2, 6, and 12 years (0.2, 0.6, and 1.2 % PVI) for MHFE-DG simulation on 80 × 80 × 80 grid (example 7)

Author's personal copy

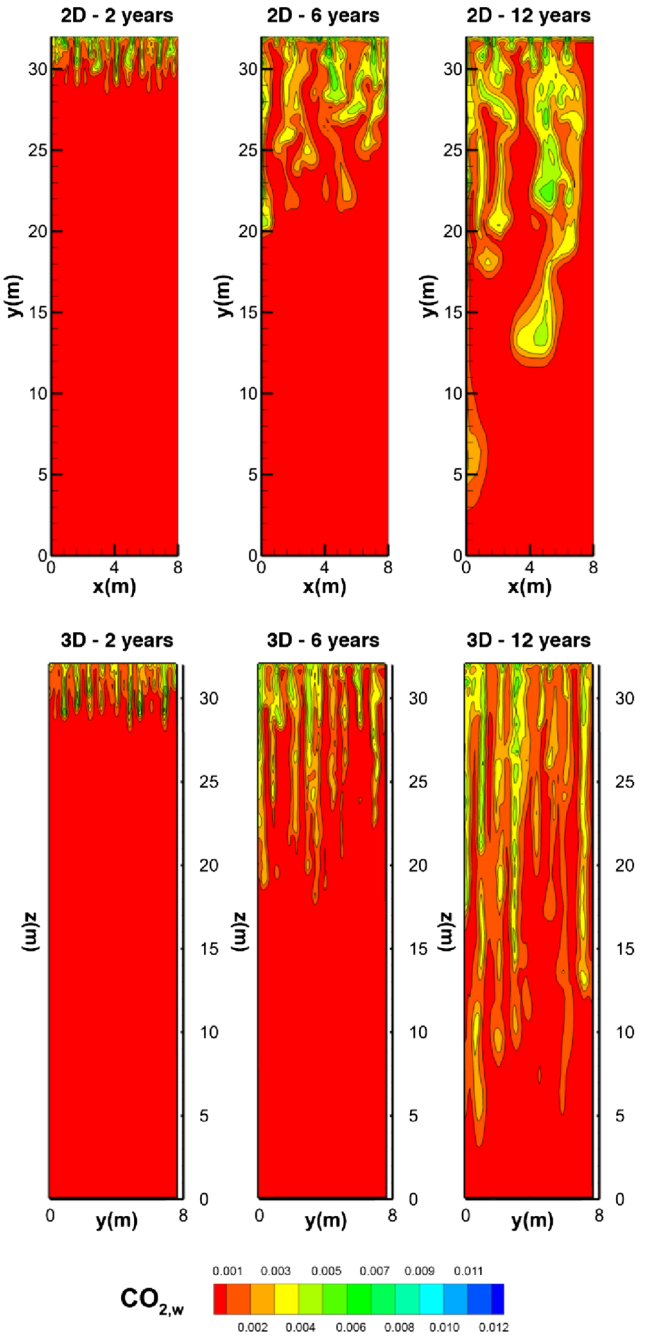

Fig. 17 CO_2 concentration in the aqueous phase (mole fraction) after 2, 6, and 12 years (0.2, 0.6, and 1.2 % PVI) 892 for MHFE-DG simulations on a 80×80 2D grid versus a $80 \times 80 \times 80$ 3D grid, cross-cut at $x = 5$ m (example 7)

CO_2 solubility is 1.7 mol%, and the CO_2-saturated aqueous phase density is 987 kg/m^3 (a 0.5 % increase). The diffusion coefficient is $D = 1.33 \times 10^{-8}$ m^2/s ($\varphi D = 2 \times 10^{-9}$ m^2/s).

The boundary conditions in our model are different from those in [10]: we consider impermeable boundaries on all sides, and inject CO_2 uniformly from the top at a constant rate of 0.1 % PV/year (at the initial pressure of 100 bar). This allows us to study the pressure buildup when CO_2 is sequestered without production. The aqueous phase density is modeled with the cubic-plus-association EOS, which takes into account the self-association and cross-association of (polar) H_2O and CO_2 molecules.

Despite the differences in boundary conditions, flow equations (compressible versus incompressible in [10]), and fluid properties (from our EOS), our simulation results are qualitatively remarkably similar to [10] (see Fig. 16). The onset of gravitational fingering (critical time) occurs after about 1 year, well-defined fingers are visible after 2 years, the number of fingers in each direction (related to the critical wavelength) is around 10–13, and the largest fingers reach the bottom of the domain after about 12 years. We also see the commonly observed tip-splitting of several of the fingers.

A noticeable difference with respect to [10] is that we do not see flattening of the fingers into sheet-like structures, but rather the fingers retain more of their axial symmetry. Both could in theory be due to grid sensitivity to structured grids, but we have found the same cylindrical finger shapes on fine tetrahedral unstructured grids, as well as in the previous example for gas-oil two-phase flow We note that a similar number of fingers as in [10] and thinner fingers at later times is observed, despite the fact that our characteristic grid dimensions are 10 cm in the top, versus 8 mm in [10]. This is a testament to the accuracy of our higher-order mass transport update, which can resolve the critical wavelength with only a few elements.

Figure 17 shows a comparison of our 3D results to an equivalent 2D simulation on a 80×80 grid with refinement in the vertical direction (the same as for the 3D grid). The 3D fingering patterns are quite different for different cross-sections (see Fig. 16) and are shown in Fig. 17 at $x = 5$ m. At the onset, the number of fingers is similar in both 2D and 3D, as predicted by linear stability theory. Interestingly, at later times the fingers are thinner and appear to propagate faster in the 3D simulation. This might be expected. A 3D pencil-like finger would be more unstable than a folded-sheet-type finger, which is the extension of the 2D simulation into the (assumed) invariant third dimension. If numerical dispersion played a role, one would expect the fingers to be larger (more dispersed) in 3D.

5 Conclusions

This work presents 3D compositional modeling based on the combined discontinuous Galerkin and mixed hybrid finite

Author's personal copy

element methods as a favorite approach for the simulation of complex fluid flow pattern formation like fingering dynamics in porous media. The model can be applied to a broad range of problems and processes.

We draw the following main conclusions from this work:

1. In 3D, the higher-order finite element framework provides twice the convergence rate of the zero-order method (Fig. 3). For a given accuracy, MHFE-DG allows significantly coarser grids or orders of magnitude improvement in CPU time (Fig. 4 shows more than three orders of magnitude improvement in CPU time for a three-phase, eight-component simulation in the simple geometry of Fig. 1).
2. Approximation of 3D compositional problems by 2D simulations may lead to different flows and different recoveries, both in the interpretation of laboratory experiments and at large scales (examples 5–7).
3. Gravity fingering in 3D can be captured by our higher-order method, whereas zero-order finite difference methods may be extremely costly when used in fingering studies (examples 5 and 6).

Acknowledgments This work is supported by the members companies of the Reservoir Engineering Research Institute (RERI). Their support is greatly appreciated.

Nomenclature

φ [−]	Porosity
t[s]	Time
p[Pa]	Pressure
$\mathbf{g}$ [kg/m/s^2]	Gravity
$\mathbf{v}$ [m/s]	Total velocity
$\phi_{K,l}(\mathbf{x})$	Linear bases functions
L_x, L_y, L_z [m]	Element K dimensions
$\mathbf{w}_{K,E}$ $(\mathbf{x})$	Raviart–Thomas linear basis vector
$\mathbf{n}_{K,E}$	Outer normal of face E of element K
C_f[m.s^2/kg]	Total compressibility
C [mol/m^3]	Overall molar density
$\alpha = o, g, w$	Generic phase
c_α [mol/m^3]	Phase α molar density
S_α [−]	Phase α saturation
$\mathbf{v}_\alpha$ [m/s]	Phase α velocity
$D_{\alpha ij}$ [m^2/s]	Fickian diffusion coefficient
λ_α [m.s/kg]	Phase α mobility
M_i [g/mol]	Molecular weight of comp$i$
f_α [−]	Fractional flow functions of phase α
$\bar{v}_I$ [m^3/mol]	Comp. i total partial molar volume
z_i[−]	Overall mole fraction of component i
$\mathbf{U_i}$ [mol/m^2/s]	Total molar flux of component i
F_i [mol/m^3/s]	Sources/sinks of component i
$\mathbf{J}_{\alpha i}$ [mol/m^2/s]	Diffusive flux of comp i in phase α
$x_{\alpha I}$[−]	Mole fraction of component i in phase α
ρ_α [kg/m^3]	Mass density of phase α
$\underline{K}$ [m^2]	Medium intrinsic permeability tensor
$k_{r\alpha}$ [−]	Phase α relative permeability
μ_α [kg/m/s]	Phase α viscosity

Appendix A: Scalar and vector basis functions in 3D

The four independent linear basis functions $\phi_{K,l}(\mathbf{x})$ in (12) are

$$\begin{aligned}
\varphi_{K,1}(x,y,z) &= 1\\
\varphi_{K,2}(x,y,z) &= \frac{2}{L_x}\left(x-\frac{L_x}{2}\right)\\
\varphi_{K,3}(x,y,z) &= \frac{2}{L_y}\left(y-\frac{L_y}{2}\right)\\
\varphi_{K,4}(x,y,z) &= \frac{2}{L_z}\left(z-\frac{L_z}{2}\right)
\end{aligned} \tag{A-1}$$

where L_x, L_y and L_z are the width, length and height of element K for a trilinear approximation.

Similarly $\mathbf{w}_{K,E}$ $(\mathbf{x})$ in (13) is the lowest-order Raviart–Thomas linear basis vector of face E in an element K:

$$\begin{aligned}
\mathbf{w}_{K,1} &= \left(\frac{x}{|K|}\ 0\ 0\right), \quad \mathbf{w}_{K,2} = \left(\frac{x-L_x}{|K|}\ 0\ 0\right)\\
\mathbf{w}_{K,3} &= \left(0\ \frac{y}{|K|}\ 0\right), \quad \mathbf{w}_{K,4} = \left(0\ \frac{y-L_y}{|K|}\ 0\right)\\
\mathbf{w}_{K,5} &= \left(0\ 0\ \frac{z}{|K|}\right), \quad \mathbf{w}_{K,6} = \left(0\ 0\ \frac{z-L_z}{|K|}\right)
\end{aligned} \tag{A-2}$$

in which $|K|$ is the volume of the element and indices 1 to 6 denote the six faces.

Appendix B: MHFE coefficients

The coefficients in (15) are

$$a_{K,E} = \lambda_t \sum_{E'\in\partial K} A^{-1}_{K,E,E'} \tag{B-1}$$

$$b_{K,E,E'} = \lambda_t A^{-1}_{K,E,E'} \tag{B-2}$$

$$d_{K,E} = \lambda_t \rho \underline{K}\mathbf{g}\cdot\mathbf{n}_{K,E}|E| \tag{B-3}$$

Author's personal copy

$A^{-1}_{K,E,E'}$ and $n_{K,E}$ are defined as

$$A^{-1} = 2\underline{K}\begin{bmatrix} \frac{L_yL_z}{L_x} & 0 & 0 & 0 & 0 & 0 \\ 0 & \frac{L_yL_z}{L_x} & 0 & 0 & 0 & 0 \\ 0 & 0 & \frac{L_xL_z}{L_y} & 0 & 0 & 0 \\ 0 & 0 & 0 & \frac{L_xL_z}{L_y} & 0 & 0 \\ 0 & 0 & 0 & 0 & \frac{L_xL_y}{L_z} & 0 \\ 0 & 0 & 0 & 0 & 0 & \frac{L_xL_y}{L_z} \end{bmatrix} \tag{B-4}$$

$$\mathbf{n} = \begin{bmatrix} 1 & -1 & 0 & 0 & 0 & 0 \\ 0 & 0 & 1 & -1 & 0 & 0 \\ 0 & 0 & 0 & 0 & 1 & -1 \end{bmatrix} \tag{B-5}$$

In Eq. 16 $\mathbf{R}(N_K \times N_E)$ is a matrix with N_K rows and N_E columns with elements:

$$R_{K,E} = a_{K,E} \tag{B-6}$$

Similarly $\mathbf{M}(N_E \times N_E)$ and $\mathbf{V}(N_E)$ where N_K and N_E are the number of elements and faces in the domain, respectively and

$$M_{E,E'} = \sum_{K:E,E'\in\partial K} b_{K,E,E'} \tag{B-7}$$

$$V_E = \sum_{K:E\in\partial K} d_{K,E} \tag{B-8}$$

$a_{K,E}, b_{K,E,E'}$ and $d_{K,E}$ are defined before. $\Sigma_{K:E,E'\in\partial K}$ represents the summation over those elements that have E and E' as edge. $\Sigma_{K:E\in\partial K}$ represents summation over those elements K which have E in common.

In Eq. (17)

$$D_K = \frac{\phi_K C_{f,K}|K|}{\Delta t} + \sum_{i=1}^{n_c} \bar{v}_i \sum_E m_{i,K,E} a_{K,E} \tag{B-9}$$

$$\tilde{R}_{K,E'} = \sum_{i=1}^{n_c} \bar{v}_i \sum_E m_{i,K,E} b_{K,E,E'} \tag{B-10}$$

$$G_K = \frac{\phi_K C_{f,K}|K|}{\Delta t} p^n_K - \sum_{i=1}^{n_c} \bar{v}_i \sum_E \left(m_{i,K,E} d_{K,E} + \mathbf{s}_{i,K,E} \cdot \mathbf{n}_{K,E}\right) + |K| \sum_{i=1}^{n_c} \bar{v}_{i,K} F_{i,K} \tag{B-11}$$

$$m_i = \Sigma_\alpha c_\alpha f_\alpha x_{\alpha I} \tag{B-12}$$

$$\mathbf{s}_i = \Sigma_\alpha (c_\alpha f_\alpha x_{\alpha i} \mathbf{G}_\alpha + S_\alpha \mathbf{J}_{\alpha i}) \tag{B-13}$$

The integrals $M^K_{j,l} = \int_K \varphi_{K,j}\varphi_{K,l}$, $M^{K,E}_{j,l} = \int_K \varphi_{K,j}\mathbf{w}_{K,E}\cdot\nabla\varphi_{K,l}$, $M^E_l = \int_E \varphi_{K,l}$ in Eq. 19 can be evaluated in 3D when $j, l = 1, \ldots, 4$ and E takes six different values for the six edges of a cubic element, which result in the following matrices:

$$\mathbf{M}^K = \left[M^K_{j,l}\right] = |K| \begin{bmatrix} 1 & 0 & 0 & 0 \\ 0 & 1/3 & 0 & 0 \\ 0 & 0 & 1/3 & 0 \\ 0 & 0 & 0 & 1/3 \end{bmatrix} \tag{B-14}$$

$$\mathbf{M}^{K,1} = \left[M^{K,1}_{l,j}\right] = \begin{bmatrix} 0 & 0 & 0 & 0 \\ 1 & 1/3 & 0 & 0 \\ 0 & 0 & 0 & 0 \\ 0 & 0 & 0 & 0 \end{bmatrix},$$

$$\mathbf{M}^{K,2} = \left[M^{K,2}_{l,j}\right] = \begin{bmatrix} 0 & 0 & 0 & 0 \\ -1 & 1/3 & 0 & 0 \\ 0 & 0 & 0 & 0 \\ 0 & 0 & 0 & 0 \end{bmatrix}$$

$$\mathbf{M}^{K,3} = \left[M^{K,3}_{l,j}\right] = \begin{bmatrix} 0 & 0 & 0 & 0 \\ 0 & 0 & 0 & 0 \\ 1 & 0 & 1/3 & 0 \\ 0 & 0 & 0 & 0 \end{bmatrix},$$

$$\mathbf{M}^{K,4} = \left[M^{K,4}_{l,j}\right] = \begin{bmatrix} 0 & 0 & 0 & 0 \\ 0 & 0 & 0 & 0 \\ -1 & 0 & 1/3 & 0 \\ 0 & 0 & 0 & 0 \end{bmatrix}$$

$$\mathbf{M}^{K,5} = \left[M^{K,5}_{l,j}\right] = \begin{bmatrix} 0 & 0 & 0 & 0 \\ 0 & 0 & 0 & 0 \\ 0 & 0 & 0 & 0 \\ 1 & 0 & 0 & 1/3 \end{bmatrix},$$

$$\mathbf{M}^{K,6} = \left[M^{K,6}_{l,j}\right] = \begin{bmatrix} 0 & 0 & 0 & 0 \\ 0 & 0 & 0 & 0 \\ 0 & 0 & 0 & 0 \\ -1 & 0 & 0 & 1/3 \end{bmatrix} \tag{B-15}$$

$$\mathbf{M}^1 = \left[M^1_l\right] = \begin{bmatrix} 1 \\ 1 \\ 0 \\ 0 \end{bmatrix}, \quad \mathbf{M}^2 = \left[M^2_l\right] = \begin{bmatrix} 1 \\ -1 \\ 0 \\ 0 \end{bmatrix},$$

$$\mathbf{M}^3 = \left[M^3_l\right] = \begin{bmatrix} 1 \\ 0 \\ 1 \\ 0 \end{bmatrix}, \quad \mathbf{M}^4 = \left[M^4_l\right] = \begin{bmatrix} 1 \\ 0 \\ -1 \\ 0 \end{bmatrix},$$

$$\mathbf{M}^5 = \left[M^5_l\right] = \begin{bmatrix} 1 \\ 0 \\ 0 \\ 1 \end{bmatrix}, \quad \mathbf{M}^6 = \left[M^6_l\right] = \begin{bmatrix} 1 \\ 0 \\ 0 \\ -1 \end{bmatrix}. \tag{B-16}$$

Author's personal copy

Appendix C: Construction of phase fluxes from total flux

Calculation of the phase velocities from Eq. 10 is not trivial because of the discontinuity of $\mathbf{G}_\alpha$ and f_α on an edge. In 2D and 3D with gravity, countercurrent flow may occur among the phases, which complicates the flow field. To avoid non-matching phase velocities at the element edge, and to guarantee the continuity of phase velocities, we need to properly determine $\mathbf{G}_\alpha$ and f_α on an edge. Details of the phase velocity calculation are provided in [46]. Here we briefly outline the technique.

For phase mass densities ρ_α and ρ_β, used in $\mathbf{G}_\alpha$, we take the arithmetic average of phase densities of the neighboring cells.

For the phase mobility λ_α, in f_α, the idea is to use the value from the upwind side of the edge with respect to $\mathbf{v}_\alpha$. The problem is how to find the flow direction of $\mathbf{v}_\alpha$ a priori (note that $\mathbf{v}_\alpha$ is not available yet). The flow direction of one of the phases (either the heaviest or the lightest one, depending on the direction of the edge normal) can be found a priori. In $\mathbf{v}_\alpha = f_\alpha(\mathbf{v} + \mathbf{G}_\alpha)$, the sign of $\mathbf{v}_\alpha$ depends on the sign of $(\mathbf{v} + \mathbf{G}_\alpha)$, because $f_\alpha > 0$. For any phase α, if $\mathbf{G}_\alpha$ has the same sign as $\mathbf{v}$, then $(\mathbf{v} + \mathbf{G}_\alpha)$ has that same sign and $\mathbf{v}_\alpha$ is in the same direction as $\mathbf{v}$ and$\mathbf{G}_\alpha$. To find the direction of the other two phases, the simplest way is trial and error for the two possible directions on each edge. We first assume one of two phases in the direction of $\mathbf{v}$ and proceed with the calculation of mobilities and phase velocities. If the sign of $\mathbf{v}_\alpha$ is consistent with chosen upwind mobility, the assumed direction is correct, otherwise it should be reversed. A consistence check is that if the local mobility of the element is picked, then the velocity should be outward, while if the neighboring mobility is chosen, the resulting phase velocity should be inward.

Appendix D: Slope limiter

It is well known that for the DG method to be stable, a slope limiter is required to avoid spurious oscillations in the solution when it takes on extreme values at the nodes. The idea is to modify the solution resulting from DG after each time step so that the average value of each molar concentration is not modified, but the slopes are adjusted such that the values of concentration at any edge are between the two neighboring element average compositions. Details of the slope limiting algorithm are presented by Hoteit and Firoozabadi [44].

After each time step of the DG method, the slope limiter provides bands for $c_K z_{i,K}$ and $c_{K'} z_{i,K'}$ for each face value of $c_E z_{i,E}$ (where $E = K \cap K'$) so that the slope is manipulated for the inequalities:

$$c_K z_{i,K} \le c_E z_{i,E} \le c_{K'} z_{i,K'} \qquad i = 1, 2, ..., n_c \tag{D-1}$$

The value of overall molar concentration is then evaluated as

$$c = \sum_{i=1}^{n_c} c z_i \tag{D-2}$$

which fulfills

$$\sum_{i=1}^{n_c} c_K z_{i,K} \le c_E \le \sum_{i=1}^{n_c} c_{K'} z_{i,K'} \tag{D-3}$$

Appendix E: Flow chart of the algorithm

The computational algorithm in this work follows the following steps:

1. Provide temperature and initial pressure and overall molar concentrations of all components
2. Perform the stability and flash calculations to determine the number of phases and phase compositions at the initial pressure, temperature and overall composition at the element center and edges
3. Evaluate phase mobilities
4. Calculate diffusion coefficients and diffusion fluxes from Eq. 3
5. Assemble and solve the system (18) for the traces of pressure $p_{K,E}$
6. Evaluate the cell-averaged pressure p on each element using Eq. 17
7. Calculate the phase velocities and total velocities as described in Appendix C
8. Compute the new overall composition from one explicit Euler step of DG
9. Apply the slope limiter
10. Perform phases-split calculations to obtain phase compositions for new condition
11. Update the phase mobilities and go to step (5)

Figure 18 illustrates the IMPEC algorithm flowchart.

Author's personal copy

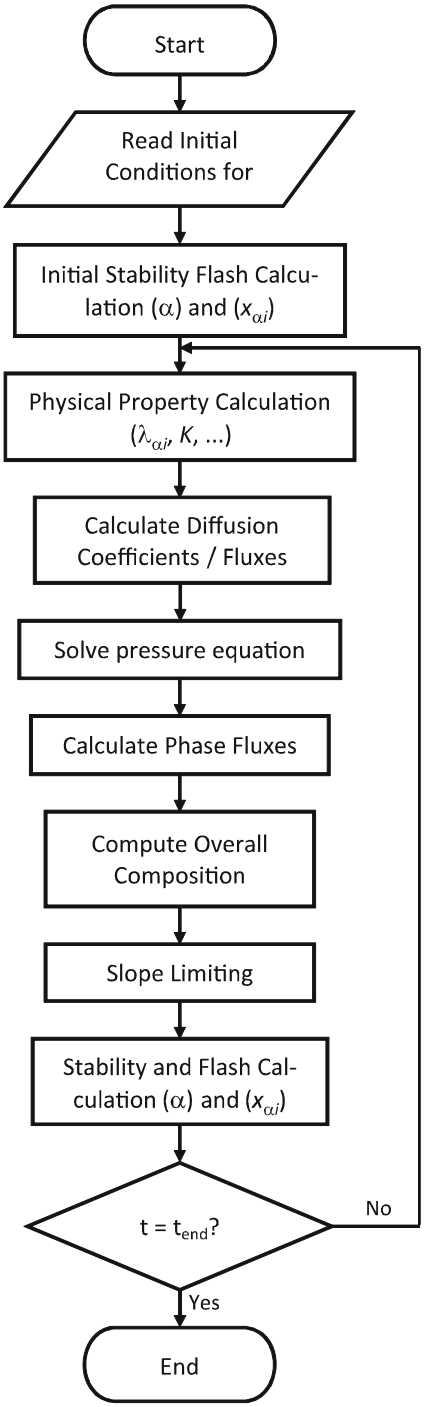

Fig. 18 Algorithm flowchart for IMPEC method

References

1. Homsy, G.M.: Viscous fingering in porous media. Annu. Rev. Fluid Mech. **19**, 271–311 (1987). doi:10.1146/annurev.fluid.19.1.271
2. DeWit, A., Homsy, G.M.: Viscous fingering in periodically heterogeneous porous media.1. Formulation and linear instability. J. Chem. Phys. **107**(22), 9609–9618 (1997). doi:10.1063/1.475258
3. DeWit, A., Homsy, G.M.: Viscous fingering in periodically heterogeneous porous media.2. Numerical simulations. J. Chem. Phys. **107**(22), 9619–9628 (1997). doi:10.1063/1.475259
4. Manickam, O., Homsy, G.M.: Simulation of viscous Fingering in miscible displacement with monotonic viscosity profiles. Phys. Fluids **6**(1), 95–107 (1994). doi:10.1063/1.868049
5. Zimmerman, W.B., Homsy, G.M.: 3-Dimensional viscous fingering - a numerical study. Phys. Fluids A: Fluid Dyn. **4**(9), 1901–1914 (1992). doi:10.1063/1.858361
6. Craster, R.V., Matar, O.K.: Dynamics and stability of thin liquid films. Rev. Mod. Phys. **81**(3), 1131–1198 (2009). doi:10.1103/RevModPhys.81.1131
7. Heussler, F.H.C., Oliveira, R.M., John, M.O., Meiburg, E.: Three-dimensional Navier-Stokes simulations of buoyant, vertical miscible Hele-Shaw displacements. J. Fluid Mech. **752**, 157–183 (2014). doi:10.1017/jfm.2014.327
8. Nittmann, J., Daccord, G., Stanley, H.E.: Fractal growth of viscous fingers - quantitative characterization of a fluid instability phenomenon. Nature **314**(6007), 141–144 (1985). doi:10.1038/314141a0
9. Oron, A., Davis, S.H., Bankoff, S.G.: Long-scale evolution of thin liquid films. Rev. Mod. Phys. **69**(3), 931–980 (1997). doi:10.1103/RevModPhys.69.931
10. Pau, G.S., Bell, J.B., Pruess, K., Almgren, A.S., Lijewski, M.J., Zhang, K.: High resolution simulation and characterization of density-driven flow in CO_2 storage in saline aquifers. Adv. Water Resour. **33**, 443–455 (2010)
11. Thompson, A.B., Juel, A., Hazel, A.L.: Multiple finger propagation modes in Hele-Shaw channels of variable depth. J. Fluid Mech. **746**, 123–164 (2014). doi:10.1017/jfm.2014.100
12. Class, H., Ebigbo, A., Helmig, R., Dahle, H.K., Nordbotten, J.M., Celia, M.A., Audigane, P., Darcis, M., Ennis-King, J., Fan, Y.Q., Flemisch, B., Gasda, S.E., Jin, M., Krug, S., Labregere, D., Beni, A.N., Pawar, R.J., Sbai, A., Thomas, S.G., Trenty, L., Wei, L.L.: A benchmark study on problems related to CO_2 storage in geologic formations. Comput. Geosci. **13**(4), 409–434 (2009). doi:10.1007/s10596-009-9146-x
13. Gerritsen, M.G., Durlofsky, L.J.: Modeling fluid flow in oil reservoirs. Annu. Rev. Fluid Mech. **37**, 211–238 (2005). doi:10.1146/annurev.fluid.37.061903.175748
14. Coats, K.H.: A note on IMPES and some IMPES-based simulation models. SPE J. **5**(3), 245–251 (2000)
15. Thomas, G.W., Thurnau, D.H.: Reservoir simulation using adaptive implicit method. SPE J. **23**, 759–768 (1983)
16. CMG: GEM (generalized equation-of-state model compositional reservoir simulator) user guide (2012)
17. Schlumberger: Eclipse technical description. In (2007)
18. Flemisch, B., Darcis, M., Erbertseder, K., Faigle, B., Lauser, A., Mosthaf, K., Müthing, S., Nuske, P., Tatomir, A., Wolff, M., Helmig, R.: DuMuX: Dune for multi-{phase, component, scale, physics,...} flow and transport in porous media. Adv. Water Resour. **34**(9), 1102–1112 (2011). doi:10.1016/j.advwatres.2011.03.007
19. Robinson, B.A., Viswanathan, H.S., Valocchi, A.J.: Efficient numerical techniques for modeling multicomponent ground-water transport based upon simultaneous solution of strongly coupled subsets of chemical components. Adv. Water Resour. **23**(4), 307–324 (2000). doi:10.1016/s0309-1708(99)00034-2
20. Cao, H.: Development of techniques for general purpose simulators. PhD, Stanford University (2002)

Author's personal copy

21. Jiang, Y.: Techniques for modeling complex reservoirs and advanced wells. PhD, Stanford University (2007)
22. Arbogast, T., Wheeler, M.F.: A characteristics-mixed finite element method for advection-dominated transport problems. SIAM J. Numer. Anal. **32**, 404–424 (1995)
23. Okuno, R., Johns, R.T., Sepehrnoori, K.: Three-phase flash in compositional simulation using a reduced method. SPE J. **15**(3), 1–15 (2010)
24. Wang, W., Kosakowski, G., Kolditz, O.: A parallel finite element scheme for thermo-hydro-mechanical (THM) coupled problems in porous media. Comput. Geosci. **35**(8), 1631–1641 (2009). doi:10.1016/j.cageo.2008.07.007
25. Wheeler, J., Wheeler, M.: Integrated parallel and accurate reservoir simulator. In. University of Texas at Austin (2001)
26. Pruess, K.: The TOUGH codes—a family of simulation tools for multiphase flow and transport processes in permeable media. Vadose Zone J. **3**(3), 738–746 (2004). doi:10.2113/3.3.738
27. Zidane, A., Firoozabadi, A.: An efficient numerical model for multicomponent compressible flow in fractured porous media. Adv. Water Resour. **74**, 127–147 (2014)
28. Jackson, M., Gomes, J., Mostaghimi, P., Percival, J., Tollit, B., Pavlidis, D., Pain, C., El-Sheikh, A., Muggeridge, A., Blunt, M.: Reservoir modeling for flow simulation using surfaces, adaptive unstructured meshes and control-volume-finite-element methods. Paper presented at the SPE Reservoir Simulation Symposium, The Woodlands, Texas, USA
29. Jackson, M., Hampson, G., El-Sheikh, A., Saunders, J., Graham, G., Massart, B.: Surface-based reservoir modelling for flow simulation. Geol. Soc. Lond. Spec. Publ., 387 (2013)
30. Blunt, M., Rubin, B.: Implicit flux limiting schemes for petroleum reservoir simulation. J. Comput. Phys. **102**(1), 194–209 (1992)
31. Liu, J., Delshad, M., Pope, G.A., Sepehrnoori, K.: Application of higher order flux-limited methods in compositional simulation. J. Transport Porous Media **16**(1-29) (1994)
32. Todd, M.R., O'Dell, P.M., Hirasaki, G.J.: Methods for increased accuracy in numerical reservoir simulators. Soc. Pet. Eng. J. **12**, 515–529 (1972)
33. Mikyska, J., Firoozabadi, A.: Implementation of higher-order methods for robust and efficient compositional simulation. J. Comput. Phys. **229**, 2898–2913 (2010). doi:10.1016/j.jcp.2009.12.022
34. Coats, K.H.: An equation of state compositional model. SPE J. **20**(5), 363–376 (1980). doi:10.2118/8284-PA
35. Ewing, R.E., Heinemann, R.F.: Incorporation of mixed finite element methods in compositional simulation for reduction of numerical dispersion. Paper presented at the SPE Reservoir Simulation Symposium, San Francisco, CA, USA, 15-18 November 1983
36. Scovazzi, G., Gerstenberger, A., Collis, S.S.: A discontinuous Galerkin method for gravity-driven viscous fingering instabilities in porous media. J. Comput. Phys. **233**, 373–399 (2013). doi:10.1016/j.jcp.2012.09.003
37. Riaz, A., Hesse, M., Tchelepi, H.A., Orr, F.M.: Onset of convection in a gravitationally unstable diffusive boundary layer in porous media. J. Fluid Mech. **548**(87–111) (2006)
38. Myint, P.C., Firoozabadi, A.: Onset of convection with fluid compressibility and interface movement. Phys. Fluids **25**, 094105 (2013)
39. Myint, P.C., Firoozabadi, A.: Onset of buoyancy-driven convection in Cartesian and cylindrical geometries. Phys. Fluids **25**, 044105 (2013)
40. Moortgat, J., Li, Z., Firoozabadi, A.: Three-phase compositional modeling of CO_2 injection by higher-order finite element methods with CPA equation of state for aqueous phase. Water Resour. Res. **48**, W12511 (2012). doi:10.1029/2011WR011736
41. Moortgat, J., Firoozabadi, A.: Fickian diffusion in discrete-fractured media from chemical potential gradients and comparison to experiment. Energy Fuel **27**(10), 5793–5805 (2013). doi:10.1021/ef401141q
42. Leahy-Dios, A., Firoozabadi, A.: Unified model for nonideal multicomponent molecular diffusion coefficients. AIChE J. **53**(11), 2932–2939 (2007)
43. Darlow, B.L., Ewing, R.E., Wheeler, M.: Mixed finite element methods for miscible displacement in porous media. Paper presented at the 6th SPE Reservoir Simulation Symposium, New Orlean, LA, USA
44. Hoteit, H., Firoozabadi, A.: Simple phase stability-testing algorithm in the reduction method. Aiche J. **52**(8), 2909–2920 (2006). doi:10.1002/aic.10908
45. Acs, G., Doleschall, E., Farkas, E.: General purpose compositional model. SPE J. **25**(4), 543-553 (1985). doi:SPE-10515-PA
46. Moortgat, J., Sun, S., Firoozabadi, A.: Compositional modeling of three-phase flow with gravity using higher-order finite element methods. Water Resour. Res. **47**, W05511 (2011). doi:10.1029/2010WR009801
47. Li, Z., Firoozabadi, A.: General strategy for stability testing and phase-split calculation in two and three phases. SPE J. **17**(4), 1096–1107 (2012). doi:SPE-129844-PP
48. Robinson, P.eng., D.-Y.: The characterization of the heptanes and heavier fractions for the GPA Peng-Robinson programs. Gpa Research Report / Rr : 28. Gas Processors Association, Tulsa, Okla (1978)
49. Li, Z., Firoozabadi, A.: Cubic-Plus-Association (Cpa) Equation of state for water-containing mixtures: is 'cross association' necessary? AIChE J. **55**(7), 1803–1813 (2009)
50. Stone, H.: Probability model for estimating three-phase relative permeability. J. Petrol. Technol. **214**, 214–218 (1970)
51. Stone, H.: Estimation of three-phase relative permeability and residual oil data. J. Can. Petrol. Technol. **12**, 53–61 (1973)
52. Hoteit, H., Firoozabadi, A.: Compositional modeling by the combined discontinuous Galerkin and mixed methods. SPE J. **11**(1), 19–34 (2006). doi:10.2118/90276-PA
53. Hoteit, H., Ackerer, P., Mose, R., Erhel, J., Philippe, B.: New two-dimensional slope limiters for discontinuous Galerkin methods on arbitrary meshes. International Journal for Numerical Methods in Engineering **61**(14), 2566–2593 (2004). doi:10.1002/nme.1172
54. Birkhoff, G., Rota, G.-C. Ordinary differential equations, 6th edn. Wiley, New York (1989)
55. Hoteit, H., Firoozabadi, A.: An efficient numerical model for incompressible two-phase flow in fractured media. Adv. Water Resour. **31**(6), 891–905 (2008). doi:10.1016/j.advwatres.2008.02.004
56. Moortgat, J., Firoozabadi, A., Li, Z., Esposito, R.: CO_2 injection in vertical and horizontal cores: measurements and numerical simulation. SPE J. **18**(2), 331–344 (2013)
57. Moortgat, J., Firoozabadi, A.: Three-phase compositional modeling with capillarity in heterogeneous and fractured media. SPE J. (2013)
58. Moortgat, J., Firoozabadi, A.: Higher-order compositional modeling of three-phase flow in 3d fractured porous media based on cross-flow equilibrium. J. Comput. Phys. **250**, 425–445 (2013). doi:10.1016/j.jcp.2013.05.009
59. Ahmed, T., Nasrabadi, H., Firoozabadi, A.: Complex flow and composition path in CO_2 injection schemes from density effects. Energy Fuel **26**, 4590–4598 (2012). doi:10.1021/ef300502f